



Deposited via The University of Leeds.

White Rose Research Online URL for this paper:

<https://eprints.whiterose.ac.uk/id/eprint/197996/>

Version: Accepted Version

---

**Article:**

Sarkar, AD and Huuse, M (2023) Subsurface temperature from seismic reflections: Application to the post-breakup sequence offshore Namibia. AAPG Bulletin, 107 (2). pp. 311-330. ISSN: 0149-1423

<https://doi.org/10.1306/10102221134>

---

© 2023. The American Association of Petroleum Geologists. All rights reserved. This is an author produced version of an article published in AAPG Bulletin. Uploaded in accordance with the publisher's self-archiving policy.

**Reuse**

Items deposited in White Rose Research Online are protected by copyright, with all rights reserved unless indicated otherwise. They may be downloaded and/or printed for private study, or other acts as permitted by national copyright laws. The publisher or other rights holders may allow further reproduction and re-use of the full text version. This is indicated by the licence information on the White Rose Research Online record for the item.

**Takedown**

If you consider content in White Rose Research Online to be in breach of UK law, please notify us by emailing [eprints@whiterose.ac.uk](mailto:eprints@whiterose.ac.uk) including the URL of the record and the reason for the withdrawal request.

5 Subsurface temperature from seismic reflections:  
6 application to the post break up sequence offshore

7 **Namibia**

8 **Arka Dyuti Sarkar**<sup>1</sup> (arkadyuti.sarkar@manchester.ac.uk) – *Corresponding author*

9 **Mads Huuse**<sup>1</sup> (mads.huuse@manchester.ac.uk)

10 <sup>1</sup>Department of Earth and Environmental Sciences, The University of Manchester,  
11 Williamson Building, Oxford Road, Manchester, M13 9PL.

12 **Acknowledgements**

13 The authors would like to thank Serica Energy and Spectrum ASA (now TGS) for provision of  
14 seismic data utilised as part of this research. We would like to thank Schlumberger for the  
15 provision of the Petrel licenses. The authors would like to thank two anonymous reviewers  
16 and editor Robert Merrill for their feedback and comments that helped improve the quality  
17 of the manuscript. We would also like to thank Kofi Owusu, Andrew Newton, David Hodgetts,  
18 and Benedict Campbell for their assistance with key sections of the project. Thanks also go to  
19 ADS's parents for their generous funding of his research.

20 **Abstract**

21 Accurate estimations of present-day subsurface temperatures are of critical importance to  
22 the energy industry, in particular with regards to geothermal energy and petroleum  
23 exploration. In frontier basins, the subsurface temperature regime can give an indication of  
24 the hydrocarbon potential of source horizons. The Lüderitz Basin, offshore Namibia, is a

25 frontier deep water basin located on a volcanic passive margin. With only two wells drilled in  
26 the area, there are limited downhole temperature data available with which to constrain the  
27 hydrocarbon window of key source rock intervals. However, high quality seismic data are  
28 available and, by applying the reflection seismic thermometry (RST) process, provides a  
29 remote sensing alternative to direct temperature measurements at high spatial resolution.  
30 Using seismic reflection and velocity data, firstly the identification of a gas hydrate bottom  
31 simulating reflector is used to derive a shallow heat flow proxy (averaging  $64 \text{ mW m}^{-2}$ ).  
32 Deriving subsurface thermal conductivity from velocity data using an empirical relationship,  
33 a prediction for subsurface temperature can be made through forward modelling. Results  
34 indicate that average temperatures at the base of the Aptian Kudu Shale interval are  $134 \text{ }^\circ\text{C}$ ,  
35 placing the source in the gas generative window within the study area. This case study  
36 demonstrates the power of RST to generate indicative subsurface temperature results in  
37 frontier exploration basins, thereby reducing uncertainty over source rock maturity prior to  
38 drilling.

## 39 Introduction

40 Subsurface temperature is a key parameter in subsurface energy extraction from petroleum-  
41 and geothermal systems (Harper, 1971; Thompson, 1979; Hunt, 1984; Bonté et al., 2012).  
42 Accurate estimations of present-day subsurface temperatures are thus of critical importance  
43 to the energy industry. In frontier areas, petroleum source rock maturity is a key uncertainty  
44 and without access to bottom hole temperature (BHT) readings from boreholes, source rock  
45 characterisation is reliant on estimation and extrapolation. A crucial component of  
46 understanding the subsurface temperature field is how heat is transferred (i.e. heat flow and  
47 thermal conductivity) (Sclater et al., 1980). Often there is limited understanding of the

48 variation in thermal conductivity both vertically and laterally in the subsurface domain due to  
49 the difficulty collecting such data. Prior to entry into frontier basins, it is advantageous to  
50 determine the generative potential of the source rock in the area. This is primarily controlled  
51 by two factors namely source rock type and temperature history. Specifically, source rock  
52 type refers to the organic matter type (marine or terrestrial), the richness of the organic  
53 matter and the content (Magoon and Dow, 1994; McCarthy et al., 2011). Source rock quality  
54 and therefore petroleum prospectivity in a basin may be ascertained through geochemical  
55 analyses such as fingerprinting for key biomarkers from oil seeps for example (Burton et al.,  
56 2018, 2019). The temperature and pressure conditions that the organic matter is subjected  
57 to, as well as the duration of temperature and pressure exposure, govern the degree of  
58 biodegradation into varying types of hydrocarbons. Along many passive margins the source  
59 rocks are at maximum burial depth and thus maximum temperature at the present day.  
60 Present day subsurface temperatures are typically acquired from temperature probe  
61 measurements that have been acquired in boreholes (Fuchs and Balling, 2016). To estimate  
62 heat flow and temperature information in adjacent areas often involves the deployment of  
63 multiple seafloor probes prior to the drilling stage (Davis et al., 2003). This then requires the  
64 extrapolation of data from nearby boreholes using structural and stratigraphic models (Davies  
65 and Davies, 2010). This methodology underutilises the available seismic datasets that are  
66 often acquired during the early stages of exploration in frontier basins. This paper presents a  
67 reflection seismic thermometry (RST) workflow for using seismic reflection data to estimate  
68 subsurface temperature before drilling and applies this to a frontier exploration setting.

69 It has been shown that gas hydrate identification on seismic reflection data through detection  
70 of bottom simulating reflectors (BSRs) at the base of gas hydrate stability zone (GHSZ), can be

71 used for geothermal gradient estimation (Yamano et al., 1982; Calvès et al., 2010; Hodgson  
72 et al., 2014; Serié et al., 2017).

73 RST predicts subsurface temperatures by first estimating surface heat flow from BSRs and  
74 then utilizing seismic processing velocities to derive thermal conductivity through an  
75 empirical transform. This empirical relationship relating acoustic velocity and thermal  
76 conductivity is a key component in allowing the estimation of subsurface temperatures  
77 throughout the seismic volume.

78 **Figure 1**

### 79 *Geological setting*

80 The study area (Fig. 1) is in the Lüderitz Basin offshore Namibia, bounded by the Orange Basin  
81 to the south, and the Walvis Basin to the north. It is part of the southern West African  
82 continental margin. Successive rifting events from the Carboniferous onwards preceded the  
83 Mesozoic opening of the South Atlantic, and the breakup of Gondwana (Bagguley and Prosser,  
84 1999; Karner and Driscoll, 1999; Schmidt, 2004). The margin offshore Namibia is characterised  
85 as having characteristics of both volcanic passive margin and non-volcanic margin end  
86 members (Light et al., 1993; Gladczenko et al., 1998; Bauer et al., 2000). Asymmetric rifting  
87 has resulted in significant variability in the sedimentary and subsidence history between the  
88 conjugate margins with this reflected in the nature of hydrocarbons discovered in these areas  
89 (Mello et al., 2011). The formation of the Walvis Ridge is contemporaneous with the extrusion  
90 of the Etendeka continental flood basalts and acted as a long-lived barrier to marine flow,  
91 creating restricted marine conditions to the north. These conditions promoted the formation  
92 of salt basins north of the Ridge in the Albian-Aptian, and these are observed on both the  
93 West African and Brazilian margins (Berger et al., 1998; Davison et al., 2012). In the Lüderitz

94 Basin multiple features such as seaward dipping reflectors (SDRs) and mass transport deposits  
95 (MTDs) can be observed (Torsvik et al., 2009) (Fig. 2 b,c). There are however no seamounts  
96 within 50 km (~31.1 mi) from the study area, the outer limit for hydrothermal systems to  
97 extend from such a system (Sclater et al., 1980; Hasterok et al., 2011).

98 The neighbouring Orange and Walvis Basins both possess working petroleum systems with  
99 gas condensate discovered in the Kudu wells and oil in the Wingat well respectively (Fig. 1)  
100 (Intawong et al., 2015). The key source interval relevant for the Lüderitz Basin is the Aptian  
101 age Kudu shale (Fig. 2). The source maturity of this interval in the Lüderitz Basin is as yet  
102 uncertain.

103 **Figure 2**

104

## *Gas Hydrates & Bottom Simulating Reflectors*

105 A BSR is traditionally considered as a continuous and coherent seismic event that cross-cuts  
106 the primary sedimentary features, whilst mimicking the morphology of the seabed (Calvès et  
107 al., 2008; Le et al., 2015; Ruppel and Kessler, 2017; Schicks, 2018). A BSR with reverse polarity  
108 and near-parallelism relative to the seabed originates from the negative acoustic impedance  
109 (AI) contrast between partially frozen, gas-hydrate bearing sediment at the base of the GHSZ  
110 and the underlying zone of dissociated free gas and water bearing sediment (Kvenvolden &  
111 Lorenson, 2001; Paganoni et al., 2016). This variant of a BSR has been commonly noted in  
112 studies globally and is usually considered a sign of hydrate presence (Shiple and Houston,  
113 1979; Stoll and Bryan, 1979; Haacke et al., 2007).

114

## *Heat Flow*

115 Understanding heat flow is crucial to building reliable geological models of both the shallow  
116 and deep subsurface and has important implications for the exploration and development of  
117 natural resources such as petroleum (Tissot et al., 1987). Heat flow has traditionally been  
118 associated with tectonism and the thickness of the radiogenic crust. However, mantle  
119 processes in continental margins also impact heat flow (Goutorbe et al., 2011). Heat from the  
120 mantle or primordial heat is one contributing factor to the thermal structure in sedimentary  
121 basins and is the deepest source of heat production (Hokstad et al., 2017). Mantle heat flow  
122 is estimated from the base of the crust, equivalent to the Moho (thus the prevalence of the  
123 1330 °C (2426 °F) isotherm as a reference point in traditional bottom-up basin modelling  
124 workflows). The other contribution to heat is in the form of radiogenic heat production.  
125 Radiogenic elements are found in insignificant quantities in oceanic crust and lithospheric

126 mantle, therefore the radiogenic heat input will be greatest in areas of continental crust and  
127 sediments (Hasterok, 2010; Allen and Allen, 2013). Basins located in the transitional zone  
128 between onshore and offshore regions tend to have considerable structural variability and  
129 thus as a consequence have been the least predictable for heat flow using global averages  
130 only (Jaupart et al., 2016; Hokstad et al., 2017). Though young ocean crust is particularly  
131 susceptible to hydrothermal fluid circulation impacting heat flow, in the Lüderitz Basin this is  
132 not an issue due to the relative age of the underlying crust and proximity to the coast parallel  
133 continent ocean boundary (COB) (Lister, 1972; Gladchenko et al., 1998).

134 Global coverage of heat flow data is not extensive, with surface heat flow data globally being  
135 limited relative to estimates of total heat output (Gosnold & Panda, 2002; Lucazeau, 2019;  
136 Macgregor, 2020). In the study area, the solitary heat flow data point is from Ocean Drilling  
137 Program (ODP) Site 1084 as shown in Fig. 1. Reported values of heat flow in published  
138 literature are made either through direct measurement or through estimations based on  
139 crustal thickness and age (Davies and Davies, 2010; Davies, 2013). Such heat flow estimates  
140 can have a threefold basis with primary data from measured data points; in oceanic crustal  
141 settings, heat flow is based on crustal thickness to mitigate for measurement perturbation  
142 due to fluid flow; and finally in the absence of measurements an estimate can be made on  
143 the basis of geology. The Bullard method is commonly used to calculate heat flow from  
144 borehole data from the relation between temperature and the thermal resistance of the  
145 sediments (Bullard, 1939; Pribnow et al., 2000). For there to be a linear relationship between  
146 acoustic velocity and thermal conductivity conditions downhole must be conductive, steady  
147 state and with no internal heat sources. The latter is difficult as heat is introduced into the  
148 system during drilling from friction with the drill bit and the circulation of drilling fluids, thus  
149 necessitating time-based corrections for the impact of drilling on local thermal regime.

## *Conventional thermal data*

150

151 Over large regions like continental margins, it is difficult to ensure high spatial resolution of  
152 thermal data from conventional techniques such as downhole temperature measurements  
153 and gravity driven thermal probes (Phrampus et al., 2017). This is both a result of scarcity of  
154 boreholes and prohibitive expense. Heat flow derived from the seismic imaging of gas  
155 hydrates can be useful in areas where significant bottom water temperature (BWT)  
156 fluctuation adversely affects the reliability of thermal probe data or where hard ground may  
157 prevent probe insertion (Hyndman et al., 2001). ODP thermal conductivity measurements on  
158 core samples from gas hydrate provinces are unreliable due to gas exsolution during recovery  
159 (Phrampus et al., 2017). This phenomenon depresses onboard thermal conductivity  
160 measurements. For the transient line source needle probe used in ODP studies to measure  
161 thermal conductivity it is important to note the orientation of the needle insertion relative to  
162 the sediment bedding direction as the thermal conductivity measurement is provided for a  
163 plane perpendicular to the needle axis (Pribnow et al., 2000). For shipboard temperature  
164 measurements temperature-time curves are subjectively fit to APC probe data (to restore to  
165 equilibrium temperatures and negate the effect of frictional heating upon insertion of the  
166 probe) (Grevemeyer and Villinger, 2001).

167 The Curie isotherm is a common subsurface thermal marker sometimes representing a  
168 petrophysical boundary (Langel and Hinze, 1998). It is commonly considered to be  $\sim 580^{\circ}\text{C}$  ( $\sim$   
169  $1076^{\circ}\text{F}$ ) as this is the Curie Point temperature of magnetite, the most common magnetic  
170 mineral in the continental crust, especially in deeper regions (Frost and Shive, 1986). Thus,  
171 the depth corresponding to a lack of magnetism is likely at temperatures in excess of the Curie  
172 point of magnetite or a result of compositional changes leading to magnetite poor rocks at

173 depth (Beardsmore and Cull, 2001). However, this method simply defines a solitary  
174 subsurface isotherm over a great depth interval from the seabed, thus making any linear  
175 geothermal gradient calculated greatly simplified. Furthermore, for high resolution  
176 estimation of the Curie isotherm depth, regional scale magnetic data would be required.  
177 Global thermal data coverage may also suffer from spatial bias (for example, shelf vs deep  
178 water settings), as there tends to be a greater interest for scientists in areas of higher heat  
179 flow resulting in a greater concentration of data, with another potential driving factor being  
180 interest in areas with geothermal energy application (Davies, 2013).

## 181 Data

### 182 *Seismic data*

183 This study uses a combination of 2D and 3D multichannel, post-stack, time-migrated seismic  
184 reflection data from offshore Namibia, covering both the shallow- and deep-water sectors of  
185 the Lüderitz basin (Fig. 1). The seismic database is correlated with a single exploration well  
186 located on the continental shelf, in addition to ODP Site 1084 in the deep-water area.

187 The 2D seismic data were provided by Spectrum ASA and consists of two surveys conducted  
188 in 2006 and 2012 respectively, with further reprocessing in 2012 (to improve image quality in  
189 legacy data and to tie 2006 vintage seismic to newly shot 2012 seismic data), and a combined  
190 total line length of 752 km (~467 mi). The lines have a 4 ms two-way travel time (TWT) sample  
191 rate. The frequency range is 3 - 206 Hz (dominant frequency ~90 Hz) with a common mid-  
192 point (CMP) spacing of 12.5 m (~41 ft) and a shot interval of 25 m (~82 ft). 2006 vintage 2D  
193 seismic data was collected with a streamer length of 8100 m (~26575 ft) while 2012 vintage  
194 2D seismic data was collected with a streamer length of 10500 m (~34449 ft).

195 The 3D seismic survey covers an area of 4150 km<sup>2</sup> (~1602 mi<sup>2</sup>) and was acquired for Serica  
196 and partners by Polarcus in 2012 using *M/V Polarcus Nadia*. Primary objective of the survey  
197 was to establish prospectivity by mapping pinch out structures and a large channel feature in  
198 the study area. Streamer length was 8100 m (~26575 ft) with 50 m (~164 ft) source separation  
199 of dual source (0.0695 m<sup>3</sup> [2.45 ft<sup>3</sup>]) air guns. It is 80-fold with a 4 ms TWT sample rate and  
200 Inline spacing of 12.5 m (~41 ft) and Xline spacing of 25 m (~82 ft). 3D pre-stack time migration  
201 was conducted by ION GXT. The isotropic frequency range for Kirchhoff pre-stack time  
202 migration (PreSTM) ranged between 3-110 Hz. All data were processed through stack and  
203 time migration. Velocity model building was done using two iterations of dense residual move  
204 out (RMO) auto-picking to create a smooth velocity model constrained by the geological  
205 horizons. Velocity model parameters include a 4 ms sample interval, 9000 ms trace length  
206 and a 6000 m (~19685 ft) aperture. By parameterising the final velocity model (Fig. 3) for  
207 steep dips and high frequency gathers, the amplitude preserving PreSTM resulted in high  
208 resolution image gathers and a very high quality final PreSTM seismic image and a high  
209 quality, if smooth, velocity model

210 **Figure 3**

211

## *Well data*

212 Well data included ODP Site 1084 and Norsk Hydro Exploration well 2513/8-1 (Fig. 1). The  
213 ODP borehole was drilled as part of ODP Leg 175 with the primary intention of documenting  
214 the migration of the Benguela Current along the South Atlantic West African Margin (Wefer  
215 et al., 1998). It is located in a water depth of 1992 m (~6535 ft) and targeted the downslope  
216 rim of the Lüderitz depositional basin.

217 The exploration well 2513/8-1 is situated on the shelf in a water depth of 243 m (~797 ft) and  
218 targeted a Lower Cretaceous lobe in a thrust ramp graben before terminating in Barremian-  
219 Aptian age volcanic rocks at a total depth of 2553 m (~8376 ft). Some sparse BHT data points  
220 from this well provide the only available calibration for the temperature estimation workflow.

## 221 **Method**

### 222 **Figure 4**

223 The temperature estimation workflow utilised in this study is outlined in Fig. 4 and described  
224 below. The entirety of the workflow has been developed and tested using commercial  
225 software developed for the petroleum industry (Schlumberger Petrel).

226 The gas hydrate stability field can be utilised to estimate the temperature at the base of the  
227 zone of stable gas hydrates, demarcated on seismic by a BSR (Dickens and Quinby-Hunt, 1994;  
228 Sloan et al., 1998; Lu and Sultan, 2008). This in turn allows a shallow geothermal gradient  
229 across the GHSZ to be estimated and surface heat flow to be estimated (Minshull, 2011;  
230 Priyanto, 2018). The stability conditions are controlled in part by the geochemical properties  
231 of the fluids available to form clathrate hydrates, which in frontier settings with limited  
232 ground truthing are generally assumed to be average salinity (33.5 ‰) seawater and pure

233 methane (Sloan et al., 1998). Pore fluid pressure conditions are generally assumed to be  
 234 hydrostatic, equivalent to  $0.0101 \text{ MPa m}^{-1}$  ( $\sim 0.446 \text{ psi ft}^{-1}$ ). The following relationship (Eq. 1)  
 235 as defined by (Dickens and Quinby-Hunt, 1994) describes methane hydrate stability:

236 **Equation 1:** 
$$\frac{1}{T_{BSR}} = 3.79 \times 10^{-3} - 2.83 \times 10^{-4}(\log P)$$

237 where  $T_{BSR}$  is temperature at the base of GHSZ (K); and  $P$  is the corresponding pressure (MPa).

238 Assuming hydrostatic pressure at the BSR depth, temperature at the base of the hydrate  
 239 stability zone has been established:

240 **Equation 2:** 
$$T_{BSR} = ((3.79 \times 10^{-3} - 2.83 \times 10^{-4}(\log(\rho \times g \times Z_{BSR})))^{-1}) - 273$$

241 Where  $T_{BSR}$  is the temperature at GHSZ ( $^{\circ}\text{C}$ );  $\rho$  is density ( $\text{kg m}^{-3}$ ) (of seawater);  $g$  is  
 242 acceleration due to gravity ( $\text{m s}^{-2}$ ) and  $Z_{BSR}$  is the depth (m) of the BSR. It must be noted that  
 243 this is a minimum temperature estimate based on assumed stability field conditions (Dickens,  
 244 2001).

245 The National Oceanic and Atmospheric Administration (NOAA) World Ocean Atlas (WOA)  
 246 (Boyer et al., 2005) is an open source dataset containing data covering the world's oceans for  
 247 temperature, salinity, density, etc. Seabed temperature (Eq. 3) was modelled in the study  
 248 area using a synthetic hydrothermal gradient derived from the closest WOA data nodes, with  
 249 the misfit from this approach amounting to  $\pm 0.4 \text{ }^{\circ}\text{C}$  ( $\pm 0.72 \text{ }^{\circ}\text{F}$ ) across the water column.

250 **Equation 3:** 
$$T_{SEABED} = (-1.919 \ln Z + 21.899) \quad \text{if } Z \leq 200$$
  
 251 
$$T_{SEABED} = 525.65Z^{-0.714} \quad \text{if } 200 < Z < 1000$$
  
 252 
$$T_{SEABED} = -0.0007Z + 4.4905 \quad \text{if } Z \geq 1000$$

253 where  $T_{SEABED}$  is the modelled hydrothermal gradient temperature ( $^{\circ}\text{C}$ ) and  $Z$  is seabed depth  
 254 (m).

255 Given both  $T_{SEABED}$ ,  $Z_{SEABED}$  and  $T_{BSR}$ ,  $Z_{BSR}$  at any geographical locality, then the geothermal  
256 gradient ( $dT/dZ$ ) across the GHSZ at that locality is given by the following relationship.

257 **Equation 4:** 
$$\frac{dT}{dZ} GHSZ = \frac{T_{BSR} - T_{SEABED}}{Z_{BSR} - Z_{SEABED}}$$

258 Where  $dT/dZ$  is geothermal gradient ( $^{\circ}\text{C km}^{-1}$ );  $T_{BSR}$  is temperature at BSR ( $^{\circ}\text{C}$ );  $T_{SEABED}$  is seabed  
259 temperature ( $^{\circ}\text{C}$ );  $Z_{BSR}$  is depth of BSR (km);  $Z_{SEABED}$  is seafloor depth (km).

260 Alongside thermal gradient, two key thermal properties are the heat flow and thermal  
261 conductivity.

262 **Equation 5:** 
$$Q = k \times \frac{dT}{dZ}$$

263 Where  $Q$  is heat flow ( $\text{mWm}^{-2}$ );  $k$  is thermal conductivity ( $\text{W m}^{-1} \text{K}^{-1}$ ) (see Section 3.1) and  
264  $dT/dZ$  is geothermal gradient ( $^{\circ}\text{C km}^{-1}$ ).

265 Fourier's Law of heat conduction (Eq. 5) is crucial to understanding the interplay between  
266 heat flow, thermal conductivity, and geothermal gradient. Establishing a shallow linear  
267 geothermal gradient using BSRs is well established (Calvès et al., 2010; Serié et al., 2017) and  
268 studies have extrapolated this shallow geotherm for traditional basin modelling workflows.  
269 This however does not consider the thermal conductivity structure of the subsurface and how  
270 it might be possible to utilise seismic reflection velocity data to do so.

### 271 *Thermal conductivity estimation*

272 Thermal conductivity is a measure of how well heat is conducted through a material (Gu et  
273 al., 2017). Difficulty associated with measuring thermal conductivity in boreholes arise from  
274 poor contact between the measuring tool and the borehole wall (Horai, 1982). Thus,  
275 considerable attention has been devoted to determining methods for estimating thermal  
276 conductivity through more easily acquired secondary data such as seismic velocity

277 measurements. Experimental studies have shown that primary controls on thermal  
278 conductivity include mineral composition, porosity and fractures (Gegenhuber and Schoen,  
279 2012). Seismic wave velocity is also largely controlled by the same factors. Early work by  
280 (Horai, 1982) sought to correlate thermal conductivity with other physical properties such as  
281 water content, bulk density, porosity and compressional sound wave velocity. The direct  
282 approach involves deriving thermal conductivity from physical properties via empirical  
283 relationships (Zamora et al., 1993). Estimates of thermal conductivity computed directly from  
284 conventional wireline data can be accurate within  $0.2 - 0.3 \text{ W m}^{-1} \text{ K}^{-1}$  ( $\sim 0.116 - 0.173 \text{ BTU h}^{-1}$   
285  $\text{ft}^{-1} \text{ }^\circ\text{F}^{-1}$ ) when derived using empirical relationships from sonic velocity data (Hartmann et al.,  
286 2005). Such a direct approach has been utilised in this work using experimental data from  
287 existing correlation studies (Brigaud et al., 1990; Brigaud & Vasseur, 1989; Esteban et al.,  
288 2015; Griffiths et al., 1992; Gunn et al., 2005; Kukkonen & Peltoniemi, 1998; Francis Lucazeau  
289 et al., 2004; Mielke et al., 2017; Popov et al., 2003; Popov et al., 1999). This direct empirical  
290 approach derived from experimental data has also been tested by the authors in other basins  
291 (Sarkar, 2020; Sarkar and Huuse, 2022).

292 Experimental data can vary in terms of the conditions under which it was collected. Most  
293 measurements have been taken at ambient pressure and temperature conditions. Binary  
294 parameterisation of the experimental datasets allows characterisation of data points  
295 collected under similar parameters. Most studies measured thermal conductivity using the  
296 optical scanning method (Popov et al., 1999). There are fewer instances in the source datasets  
297 of the use of the divided bar method of measuring thermal conductivity (Hyndman and  
298 Jolivet, 1976; Evans, 1977). Only wet samples from these studies were used as our case study  
299 is in deep water and thus fully saturated with water, gas and/or gas hydrate. In dry samples,  
300 the contribution to thermal conductivity arising from lithological heterogeneities (matrix

301 properties) can be masked by the stronger influence of porosity (Hartmann et al., 2005). In  
302 contrast wet samples reflect the impact of porosity and lithological variations.

303 The range of samples included in our fit cover a wide range of lithologies, including  
304 sandstones, limestones, granites, basalts, marble to name a few (Grevemeyer and Villinger,  
305 2001; Hartmann et al., 2005; Boulanouar et al., 2013; Esteban et al., 2015; Jorand et al., 2015;  
306 Gu et al., 2017; Mielke et al., 2017). In so doing it is hoped that the resulting empirical  
307 relationship will best apply to the broadest possible range of rock types that can be expected  
308 subsurface across the study area. It must be noted though that variables within the sample  
309 set (Fig. 5) include and are not limited to the porosity (arising from cracks for example).  
310 Fractures are known to reduce both P wave velocities and thermal conductivity (Zamora et  
311 al., 1993).

312 A regression through the filtered experimental data points taken from the aforementioned  
313 studies gives the following empirical relationship for thermal conductivity:

314 **Equation 6:**  $k_V = (0.001 \times V_P) - 0.5071$

315 Where  $k_V$  is thermal conductivity from velocity ( $W m^{-1} K^{-1}$ ) and  $V_P$  is P wave velocity ( $m s^{-1}$ ).

316 **Figure 5**

317 Certain trends are evident in the cross plot of sample data in Fig. 5. Due to the lack of salt  
318 encountered in the study area, there is a lack of sample points in the expected high  
319 conductivities associated with salt (Esteban et al., 2015). The regression is anchored by the  
320 large cluster of points associated with the Grevemeyer & Villinger (2001) data. The Hartmann  
321 et al. (2005) and Gu et al. (2017) samples are parallel to the best fit regression.

322 Seismic P wave velocity within the area is converted to thermal conductivity ( $k_V$ ) using the  
323 thermal conductivity relationship (Eq. 6), with velocity averaged down to the depth of the

324 BSR,  $Z_{BSR}$ . The variation in thermal conductivity with depth can be overlain on a 3D seismic  
325 reflection dataset in this manner. Using  $Z_{BSR}$ , determined on reflection seismic data, the  
326 hydrate stability field can be utilised to compute the temperature at this phase boundary for  
327 the base of the GHSZ (using Eq. 2). Temperature at the seabed is known from the  
328 hydrothermal gradient (given by Eq. 3). A shallow geothermal gradient may thus be computed  
329 between seabed and BSR (Eq. 4). As thermal conductivity has been derived from acoustic  
330 velocity data, and with shallow geothermal gradient also available, it becomes possible to  
331 reapply Fourier's Law (Eq. 5) to derive heat flow for this area through inverse modelling.  
332 Estimating the shallow geotherm and heat flow along the full extent of a BSR helps eliminate  
333 the bias in heat flow distribution from direct measurements taken at discrete locations  
334 (Shankar and Riedel, 2013). This BSR derived heat flow proxy is used in conjunction with the  
335 bulk thermal conductivity volume to generate a volume of average geothermal gradient for  
336 the bulk volume (rearranging Eq. 5).

337 Temperature below the seafloor can be summarised as being a function of the depth below  
338 the seafloor and the average geothermal gradient. It follows that an estimate of temperature  
339 may be arrived at through this simple relationship where the temperature at any given depth  
340 point is given by multiplying the average geothermal gradient against the depth to that point:

341 **Equation 7:** 
$$T = T_{SEABED} + \left( \frac{dT}{dZ} \times Z_{SUBSURFACE} \right)$$

342 where  $T$  is predicted temperature ( $^{\circ}\text{C}$ );  $T_{SEABED}$  is the temperature at seabed ( $^{\circ}\text{C}$ );  $dT/dZ$  is the  
343 average geothermal gradient ( $^{\circ}\text{C km}^{-1}$ ); and  $Z_{SUBSURFACE}$  is the subsurface depth (km). Seabed  
344 temperature is added to account for the effect of the hydrothermal gradient on the  
345 subsurface temperatures.

346 As the average geothermal gradient is only valid for the subsurface and due to the seismic  
347 input volume containing the water column it becomes necessary to negate the latter. Without  
348 flattening the volume to the seabed, it is instead possible to use the seabed depth map to  
349 derive a depth volume relative to seabed depth.

350 **Equation 8:**  $Z_{SUBSURFACE} = Z - Z_{SEABED}$

351 where  $Z_{SUBSURFACE}$  is the subsurface depth (km);  $Z$  is the absolute depth (km); and  $Z_{SEABED}$  is the  
352 seabed depth (km).

353 The steps outlined above are all possible using basic functions available within the Petrel  
354 seismic interpretation suite. A pillar grid corresponding to the extent of the seismic survey is  
355 built with voxel sizes of 50 m \* 50 m \* 10 m (~164 ft \* 164 ft \* 32.8 ft). The original seismic  
356 reflection and velocity data can be resampled into the pillar grid. It must be noted that  
357 resampling the original data may result in a loss of fidelity from the algorithm used and the  
358 size of the voxels comprising the model. The advantage of using such a pillar grid is that  
359 computation of the various properties such as velocity derived thermal conductivity ( $k_v$ )  
360 become easier. It is also easier to model pseudo-wells in this manner.

### 361 *Uncertainty modelling*

362 An attempt to model uncertainty was made following the use of 95% confidence interval  
363 method as used by Phrampus et al. (2017) to derive bounds for both the heat flow proxy from  
364 BSR and the overall temperature prediction. The approach to calculating these bounds can be  
365 considered modular for the two aforementioned predicted thermal properties, with the same  
366 workflow (Fig. 4) also used here but with an upper bound and lower bound approach for each  
367 step as shown in Table 1. For example, to model the lower bound of the shallow heat flow  
368 proxy, firstly the lower bound of the root mean square (RMS) of interval velocity across the

369 GHSZ is used to domain convert the TWT BSR pick. This has the effect of varying the BSR in  
370 depth, to a shallower depth because of the lower interval velocity selected which in turn  
371 would result in a lower temperature for the BSR using the phase relationship described  
372 previously. It must be noted that the hydrate phase composition is not varied and that the  
373 pressure field is unaltered from previous modelling. Similarly, the seabed depth and  
374 temperature are considered unchanged. This gives the lower bound for geothermal gradient.  
375 Using the 1D approximation of Fourier's law (Eq. 5) this lower bound geothermal gradient is  
376 convolved with the lower bound regression for thermal conductivity from velocity separate  
377 from that discussed in Section 3.1 but based on the same 95% confidence interval. This results  
378 in the lower bound of the heat flow estimate from the BSR. Using the opposite bound of the  
379 various component steps helps arrive at the upper bound for heat flow. The bounds for the  
380 temperature prediction can be simplified to varying the bulk thermal conductivity volume and  
381 conditioning the model with the upper and lower bound heat flow from BSR. This gives an  
382 envelope of temperatures representing the spread of values possible using 95% confidence  
383 for all input parameters.  
384

385 **Table 1**

386 **Results**

387 The BSR observed in the area has been mapped across the NW and SW quadrants of the 3D  
388 reflection seismic coverage (Fig. 6). Though the full extent of the visible BSR was mapped, only  
389 the extent corresponding to the highest confidence seismic picks are displayed as the clarity  
390 of the BSR degrades towards the edges. This should preclude any resulting anomalous  
391 artefacts and edge effects. It is this high confidence extent of the BSR that is referred to in the  
392 following sections unless otherwise specified. The BSRs are found to have opposite seismic  
393 reflection polarity to the seabed reflection indicating the likelihood of gas hydrate above free  
394 gas (Kretschmer et al., 2015). Though there is no record of hydrates from ODP Site 1084, high  
395 amplitude reflections are observed to occur in close proximity below the BSR (Fig. 2a),  
396 characteristic of the presence of trapped gas. Temperature at BSR depth and the phase  
397 relationship used to determine this is shown in Fig. 6.

398 **Figure 6**

399 Neither the exploration well nor ODP Site 1084 fall within the bounds of the thermal model.  
400 As a result, direct calibration is not possible. However well 2513/8-1 contains BHT information  
401 that may provide some calibration for the predicted results. Pseudo-wells provide a means of  
402 simulating 2513/8-1 at a comparable location along strike (Fig. 1a). Pseudo-well P1 is  
403 projected into the study area following bathymetric contours as close as possible along strike  
404 from 2513/8-1, to maintain structural parity. BHT recordings typically are lower than actual  
405 formation temperature due to cooling effect of circulating fluids in a borehole and thus they  
406 must be corrected (Deming, 1989). There are insufficient points for a Horner correction  
407 (Horner, 1951; Bonté et al., 2012) to be applied and hence a rudimentary correction is made

408 for time since circulation (see <https://www.zetaware.com/utilities/bht/timesince.html> first  
409 accessed August 2018). The predicted temperatures are between 17 and 26% higher than the  
410 corrected BHT (Fig. 7a).

#### 411 **Figure 7**

412 On seismic data it was evident that there is a deeply incised canyon like structure trending NE  
413 – SW that can be seen in the north-eastern most extent of the seismic volume (Wanke and  
414 Toirac-proenza, 2018). This corresponds to the location of P1, which is seen to intersect the  
415 channel fill structures of this canyon. It becomes evident then that though P1 was projected  
416 into the seismic volume maintaining bathymetric parity, in the subsurface, due to the  
417 occurrence of this channel like geometry, it is not possible to maintain stratigraphic parity to  
418 2513/8-1. This is surmised to be the primary factor for the misfit with BHT seen.

419 Further pseudo-wells (T1 – 3) were modelled to examine the change in thermal profile moving  
420 from the proximal section to the distal part of the study area. The results (Fig. 7) display what  
421 the thermal profile in these pseudo-wells would be like if a typical geothermal gradient of 30  
422 °C km<sup>-1</sup> or 40 °C km<sup>-1</sup> (87 °F mi<sup>-1</sup> or 116 °F mi<sup>-1</sup>, respectively) was applied linearly from seabed.  
423 The temperature window considered prospective for reservoirs at the present day has been  
424 referred to as the Golden Zone (60 – 120 °C [140 – 248 °F]) (Nadeau, 2011). It becomes  
425 apparent then that the varying geothermal gradient with depth of the proposed model would  
426 significantly alter the subsurface depth at which the Golden Zone would begin and end in  
427 comparison to the typical linear geothermal gradients that are often considered in a  
428 traditional basin modelling workflow. Analysing the geothermal gradient between these  
429 pseudo-wells it is seen that in the proximal section (T1) there is a much steeper drop off (~57.1  
430 °C km<sup>-1</sup> [165 °F mi<sup>-1</sup>] in the uppermost 800 m [~2625 ft] to 15 °C km<sup>-1</sup> [43 °F mi<sup>-1</sup>] in the deepest  
431 1000 m [~3281 ft]) compared to the intermediate (T2) and deeper sections (T3). The spread

432 of isotherms in a dip section (Fig. 8) reflects this. Isotherm spacing is regular in the Mesozoic  
433 section moving into deeper water. However, in the proximal end corresponding to minimal  
434 Tertiary cover, there is observed the greatest divergence between isotherms in Mesozoic  
435 sediment. Temperature for the Aptian 'Kudu shale' source rock in the region has also been  
436 mapped (Fig. 8).

437 **Figure 8**

438 Below both BSRs, but particularly the northern BSR (Fig. 6), the effects of gas blanking were  
439 observed in the seismic reflection data. An average interval velocity extraction reveals  
440 anomalously low values within this area (Fig. 8). Pseudo-well T4 was modelled to capture this  
441 area. These results are consistent with the deep-water pseudo-well T3 with similar  
442 geothermal gradient at each 1000 m (~3281 ft) interval between the two pseudo-wells.

## 443 Discussion

### 444 *Uncertainty*

445 In a quantitative workflow such as the one discussed in the paper, there are multiple avenues  
446 for uncertainty in the constituent steps. Previous literature includes attempts to quantify the  
447 cumulative uncertainty in predictions using a BSR derived geothermal gradient (5 – 35%) and  
448 heat flow (10 – 50%) (Grevemeyer and Villinger, 2001). Such attempts have usually quantified  
449 uncertainty for the component steps rather than the compound uncertainty for the entire  
450 process. The parameter-based error in BSR heat flow could lead to a disparity of up to 25%  
451 with measured heat flow (He et al., 2009). For this work, with a lack of well data for ground  
452 truthing, the temperature estimation bounds for 95% confidence were used to give an idea  
453 of the range within which the estimates can vary. It is important to note the impact of  
454 variability in input factors for the component steps. For example, results from the Blake Ridge  
455 show that actual temperatures at the BSR depth could be between 0.5 – 2.9 °C (0.9 – 5.2 °F)  
456 lower than the temperature predicted by the hydrate phase relationship for that particular  
457 depth and pressure (Wood and Ruppel, 2000). This implies that a significant source of  
458 uncertainty in the thermal modelling could result from the assumptions made about the  
459 conditions at the base of the GHSZ. As stated earlier, an assumption has been made on the  
460 lattice fluid and trapped gas mix for the hydrate zone in the absence of direct piston core

461 sampling. Varying gas compositions can vary the hydrate stability and thus alter the  
462 temperature at the bottom simulating reflector (Chand et al., 2008). The prevalence of  
463 methane hydrates globally leads us to assume it is the most likely composition of the hydrates  
464 in the study area.

465 As the temperature dependency of gas hydrate is a key component of RST applied without  
466 direct temperature measurements, factors causing hydrate instability can also introduce  
467 uncertainty. Instability can be caused by various factors such as relatively recent warming or  
468 varying sea level, isostatic rebound, and tectonic uplift affecting the ambient pressure at the  
469 BSR (Li et al., 2017; Burton et al., 2020).

470 BWT fluctuations, both the magnitude and time scale for which they occur provide another  
471 element of uncertainty. It must be noted that the strong Benguela Current flows along the  
472 Namibian margin in this area (Putuhena et al., 2021) and it is difficult to directly factor in the  
473 impact that ocean current fluctuations may have on the modelling. The data used to generate  
474 a model of the hydrothermal gradient in the area utilised NOAA data that have been averaged  
475 annually over an eight-year period, but glacial-interglacial BWT changes are poorly known and  
476 thus difficult to factor in. Hence, in the absence of evidence to the contrary we assume the  
477 BSRs observed are in thermal equilibrium and recognise this carries an inherent uncertainty.

478 The quality of the initial velocity model is another source of uncertainty. As thermal  
479 conductivity is derived from it using a direct empirical relationship, any anomalies in the  
480 existing velocity model or velocity data will be translated into the derived properties. From  
481 the low spread of RMS interval velocities for the GHSZ it is apparent the application of a  
482 default  $1500 \text{ m s}^{-1}$  ( $\sim 4921 \text{ ft s}^{-1}$ ) velocity above seabed during the velocity model building stage  
483 results in a heavily smoothed velocity model. This is expected to be reflected in the nature of  
484 the temperature profile generated using velocities as input.

485 In this study, BSRs are used to derive the geotherm of the shallow subsurface hydrate stability  
486 field and heat flow. One of the uncertainties to this approach is the thermal conductivity of  
487 the rock column below the BSR (Burton et al., 2020). Burton et al. (2020) have shown that in  
488 a case of variable basal heat flow, BSR depth may be constant due to varying sub-BSR thermal  
489 conductivity (conversely if basal heat flow is constant, BSR depth may vary due to differences  
490 in sub-BSR thermal conductivity). In the RST approach, variability in sub-BSR thermal  
491 conductivity is accounted for in the bulk transformation of velocities to thermal conductivity.  
492 In the Blake Ridge example (Sarkar, 2020), borehole velocities available below the GHSZ were  
493 used to convert to thermal conductivity, and then used to approximate a surface heat flow  
494 proxy. If heat flow results calibrate from this approach, it would suggest that this effect has  
495 been mitigated.

496 In the absence of a reliable heat flow recording for this area, a BSR derived heat flow proxy  
497 has been used. This is a shallow heat flow as it uses an average velocity derived thermal  
498 conductivity and geothermal gradient valid within the GHSZ (Eq. 5). Unlike in traditional basin  
499 modelling the radiogenic heat production of the rock column has not been integrated.  
500 Instead, this solitary heat flow proxy has been used to condition the model for an average  
501 geothermal gradient. Though hydrothermal fluid circulation in the subsurface can also greatly  
502 alter heat flow, both vertically and laterally, the study area is likely to be minimally impacted  
503 in this regard. As the study area is sufficiently distant from a neighbouring seamount to negate  
504 the convective and advective heat flow impact of hydrothermal fluid circulation, heat  
505 transport in this area is predominantly conductive. Therefore, the assumption is of limited  
506 lateral heat flow variability, which is backed by the BSR-derived thermal gradients and  
507 derivative heat flow estimates. In a separate case study covering the data rich North Sea, it  
508 has been shown that RST can be conducted successfully using laterally varying shallow heat

509 flow as a parameter input (Sarkar, 2020). An estimate of the uncertainty of the heat flow  
510 derived in this manner has been computed using the method shown in Phrampus et al. (2017).  
511 Heat flow is found to range between 46.2 – 76.2 mWm<sup>-2</sup> (~0.01465 – 0.02416 BTU h<sup>-1</sup> ft<sup>-2</sup>),  
512 with the weighted mean for the heat flow used for computation of the temperature model  
513 equal to 64 mWm<sup>-2</sup> (~0.02022 BTU h<sup>-1</sup> ft<sup>-2</sup>). The lower bound of the derived ranged is  
514 consistent with results from Macgregor (2020) while the upper bound would be in line with  
515 the preferred prediction from the global map in Lucazeau (2019). The weighted mean is  
516 interestingly consistent with the continental margin heat flow mean reported by Davies  
517 (2013). The heat flow range given by the bounds is consistent with observational data and  
518 estimations of heat flow from age relationships corresponding to this area (Hamza and Vieira,  
519 2012).

520 The BSR expression itself may be another source of uncertainty. The BSR based thermal  
521 modelling is predicated on the understanding that its expression is along the base of the  
522 GHSZ. In some instances though, multiple stacked BSRs might be observed (Popescu et al.,  
523 2006), with gas hydrate occurring below it (Paganoni et al., 2016). These have been  
524 speculated to be paleo/relict BSRs (Hornbach et al., 2003) or a consequence of there being a  
525 mixed phase boundary (Paganoni et al., 2016). For this work, the BSR is assumed to be  
526 representative of the phase boundary for methane hydrate stability.

## 527 *Implications*

528 As stated previously, the source maturity of the Aptian Kudu Shale interval in the Lüderitz  
529 Basin is a key unknown in terms of the petroleum systems elements. With the thermal  
530 modelling workflow indicating an average temperature of 134 °C (272.3 °F) across the top of  
531 the Barremian Prospect B structure (Fig. 8a), the base of the overlying Kudu shale source rock

532 immediately above would therefore lie in the gas generation window (Bjørlykke et al., 1989).  
533 This is consistent with the nearby Kudu fields which produce gas condensate from the same  
534 Aptian source interval (Van Der Spuy, 2003; Schmidt, 2004; Samakinde et al., 2021). The  
535 results thus suggest that the Lüderitz Basin has the potential for a working hydrocarbon  
536 system with gas charged reservoirs.

537 This study estimated present day temperature at key subsurface target depths in a frontier  
538 setting in the absence of any substantive well control. The workflow presented enables  
539 seismic operators to utilise data libraries of seismic reflection and velocity data to generate  
540 present day estimations of subsurface temperature in a non-invasive manner, prior to an  
541 expensive drilling campaign. It is hoped that this will help streamline petroleum systems  
542 analysis and provide an additional dataset for basin modellers to use help minimise  
543 exploration uncertainty.

## 544 Conclusions

545 The RST model proposed in this study is a simple and robust methodology for estimation of  
546 present-day subsurface temperature in frontier areas lacking borehole control for  
547 temperatures (such as the Lüderitz Basin). It makes use of readily available seismic reflection  
548 and velocity data in a workflow developed on an industry standard software suite. It highlights  
549 how established workflows for BSR derived heat flow may be combined with existing  
550 experimental thermal conductivity and velocity data for various lithologies to develop an  
551 empirical transform that may be used to generate a thermal conductivity volume from seismic  
552 velocity models. Given thermal conductivity and P wave velocity have sensitivity to similar  
553 parameters, this methodology allows the user to examine the vertical and lateral variability  
554 in thermal properties in a frontier basin especially when high-quality pre-SDM and FWI

555 velocity models are available. Indications from RST suggest that the key Aptian source interval  
556 along this margin (the Kudu Shale) is in the gas generative window, based on an average  
557 predicted basal temperature 134 °C. The immediately underlying primary Barremian Prospect  
558 B structure is therefore deeper than the threshold temperature for the Golden Zone in  
559 reservoirs. The gas hydrate based heat flow proxy averages 64 mW m<sup>-2</sup> in this basin.

## 560 References

- 561 Allen, P., and J. Allen, 2013, Basin analysis: principles and application to petroleum play  
562 assessment.
- 563 Bagguley, J., and S. Prosser, 1999, The interpretation of passive margin depositional processes  
564 using seismic stratigraphy: examples from offshore Namibia: Geological Society, London,  
565 Special Publications, v. 153, no. 1, p. 321–344, doi:10.1144/GSL.SP.1999.153.01.20.
- 566 Bauer, K., S. Neben, B. Schreckenberger, R. Emmermann, K. Hinz, N. Fechner, K. Gohl, A.  
567 Schulze, R. B. Trumbull, and K. Weber, 2000, Deep structure of the Namibia continental  
568 margin as derived from integrated geophysical studies: Journal of Geophysical Research:  
569 Solid Earth, v. 105, no. B11, p. 25829–25853, doi:10.1029/2000JB900227.
- 570 Beardsmore, G., and J. Cull, 2001, Crustal Heat Flow: A Guide to Measurement and Modelling:  
571 doi:10.1017/S0016756803218021.
- 572 Becker, J. J. et al., 2009, Global Bathymetry and Elevation Data at 30 Arc Seconds Resolution:  
573 SRTM30\_PLUS: Marine Geodesy, v. 32, no. 4, p. 355–371,  
574 doi:10.1080/01490410903297766.
- 575 Berger, W., G. Wefer, C. Richter, C. Lange, J. Girardeau, O. Hemelin, and Shipboard Scientific  
576 Party, 1998, 17. The Angola-Benguela upwelling system: Paleoceanographic synthesis of  
577 shipboard results from Leg 175: Proceedings of the Ocean Drilling Program, v. 175, p.  
578 505–531.
- 579 Bjørlykke, K., M. Ramm, and G. C. Saigal, 1989, Sandstone diagenesis and porosity  
580 modification during basin evolution: Geologische Rundschau, v. 78, no. 1, p. 243–268,  
581 doi:10.1007/BF01988363.
- 582 Bonté, D., J. D. Van Wees, and J. M. Verweij, 2012, Subsurface temperature of the onshore  
583 Netherlands: New temperature dataset and modelling: Geologie en  
584 Mijnbouw/Netherlands Journal of Geosciences, v. 91, no. 4, p. 491–515,  
585 doi:10.1017/S0016774600000354.
- 586 Boulanouar, A., A. Rahmouni, M. Boukalouch, A. Samaouali, Y. Géraud, M. Harnafi, and J.  
587 Sebbani, 2013, Determination of Thermal Conductivity and Porosity of Building Stone  
588 from Ultrasonic Velocity Measurements: Geomaterials, v. 03, no. 04, p. 138–144,  
589 doi:10.4236/gm.2013.34018.
- 590 Boyer, T., S. Levitus, H. Garcia, R. A. Locarnini, C. Stephens, and J. Antonov, 2005, Objective  
591 analyses of annual, seasonal, and monthly temperature and salinity for the World Ocean  
592 on a 0.25° grid: International Journal of Climatology, v. 25, no. 7, p. 931–945,  
593 doi:10.1002/joc.1173.

- 594 Bray, R., S. Lawrence, and R. Swart, 1998, Namibia License Blocks , Wells: Oil and Gas Journal,  
595 v. 96, no. 32, p. 84–88.
- 596 Brigaud, F., D. S. Chapman, and S. Le Douaran, 1990, Estimating thermal conductivity in  
597 sedimentary basins using lithologic data and geophysical well logs: American Association  
598 of Petroleum Geologists Bulletin, v. 74, no. 9, p. 1459–1477, doi:10.1306/OC9B2501-  
599 1710-11D7-8645000102C1865D.
- 600 Brigaud, F., and G. Vasseur, 1989, Mineralogy, porosity and fluid control on thermal  
601 conductivity of sedimentary rocks: Geophysical Journal International, v. 98, no. 3, p. 525–  
602 542, doi:10.1111/j.1365-246X.1989.tb02287.x.
- 603 Bullard, E. C., 1939, Heat flow in South Africa: Proceedings of the Royal Society of London.  
604 Series A. Mathematical and Physical Sciences, v. 173, no. 955, p. 474–502,  
605 doi:10.1098/rspa.1939.0159.
- 606 Burton, Z. F. M., J. P. Cassanelli, T. Mukerji, and S. A. Graham, 2020, Impact of Sub-Gas Hydrate  
607 Sediment Thermal Conductivity on Hydrate-Based Heat Flow Derivations, *in* AGU Fall  
608 Meeting Abstracts: American Geophysical Union, p. OS029-0009.
- 609 Burton, Z. F. M., K. F. Kroeger, A. Hosford Scheirer, Y. Seol, B. Burgreen-Chan, and S. A.  
610 Graham, 2020, Tectonic Uplift Destabilizes Subsea Gas Hydrate: A Model Example From  
611 Hikurangi Margin, New Zealand: Geophysical Research Letters, v. 47, no. 7,  
612 doi:10.1029/2020GL087150.
- 613 Burton, Z. F. M., J. M. Moldowan, L. B. Magoon, R. Sykes, and S. A. Graham, 2019,  
614 Interpretation of source rock depositional environment and age from seep oil, east coast  
615 of New Zealand: International Journal of Earth Sciences, v. 108, no. 4, p. 1079–1091,  
616 doi:10.1007/s00531-018-01675-6.
- 617 Burton, Z. F. M., J. M. Moldowan, R. Sykes, and S. A. Graham, 2018, Unraveling Petroleum  
618 Degradation, Maturity, and Mixing and Addressing Impact on Petroleum Prospectivity:  
619 Insights from Frontier Exploration Regions in New Zealand: Energy & Fuels, v. 32, no. 2,  
620 p. 1287–1296, doi:10.1021/acs.energyfuels.7b03261.
- 621 Calvès, G., M. Huuse, A. Schwab, and P. Clift, 2008, Three-dimensional seismic analysis of high-  
622 amplitude anomalies in the shallow subsurface of the Northern Indus Fan: Sedimentary  
623 and/or fluid origin: Journal of Geophysical Research, v. 113, no. B11, p. B11103,  
624 doi:10.1029/2008JB005666.
- 625 Calvès, G., A. M. Schwab, M. Huuse, P. D. Clift, and A. Inam, 2010, Thermal regime of the  
626 northwest Indian rifted margin - Comparison with predictions: Marine and Petroleum  
627 Geology, v. 27, no. 5, p. 1133–1147, doi:10.1016/j.marpetgeo.2010.02.010.
- 628 Chand, S., J. Mienert, K. Andreassen, J. Knies, L. Plassen, and B. Fotland, 2008, Gas hydrate  
629 stability zone modelling in areas of salt tectonics and pockmarks of the Barents Sea  
630 suggests an active hydrocarbon venting system: Marine and Petroleum Geology, v. 25,  
631 no. 7, p. 625–636, doi:10.1016/j.marpetgeo.2007.10.006.
- 632 Crameri, F., G. E. Shephard, and P. J. Heron, 2020, The misuse of colour in science  
633 communication: Nature Communications, v. 11, no. 1, p. 5444, doi:10.1038/s41467-020-  
634 19160-7.
- 635 Davies, J. H., 2013, Global map of solid Earth surface heat flow: Geochemistry, Geophysics,  
636 Geosystems, v. 14, no. 10, p. 4608–4622, doi:10.1002/ggge.20271.
- 637 Davies, J. H., and D. R. Davies, 2010, Earth’s surface heat flux: Solid Earth, v. 1, no. 1, p. 5–24,  
638 doi:10.5194/se-1-5-2010.

639 Davis, E. E., K. Wang, K. Becker, R. E. Thomson, and I. Yashayaev, 2003, Deep-ocean  
640 temperature variations and implications for errors in seafloor heat flow determinations:  
641 *Journal of Geophysical Research: Solid Earth*, v. 108, no. B1, p. 1–6,  
642 doi:10.1029/2001JB001695.

643 Davison, I., L. Anderson, and P. Nuttall, 2012, Salt deposition, loading and gravity drainage in  
644 the Campos and Santos salt basins: Geological Society, London, Special Publications, v.  
645 363, no. 1, p. 159–174, doi:10.1144/SP363.8.

646 Deming, D., 1989, Application of bottom-hole temperature corrections in geothermal studies:  
647 *Geothermics*, v. 18, no. 5–6, p. 775–786, doi:10.1016/0375-6505(89)90106-5.

648 Dickens, G. R., 2001, Modeling the Global Carbon Cycle with a Gas Hydrate Capacitor:  
649 Significance for the Latest Paleocene Thermal Maximum, *in* C. K. Paull, and W. P. Dillon,  
650 eds., *Natural gas hydrates: occurrence, distribution, and detection*: Washington, D. C.,  
651 AGU, p. 19–38, doi:10.1029/GM124p0019.

652 Dickens, G. R., and M. S. Quinby-Hunt, 1994, Methane hydrate stability in seawater:  
653 *Geophysical Research Letters*, v. 21, no. 19, p. 2115–2118, doi:10.1029/94GL01858.

654 Esteban, L., L. Pimienta, J. Sarout, C. D. Piane, S. Haffen, Y. Geraud, and N. E. Timms, 2015,  
655 Study cases of thermal conductivity prediction from P-wave velocity and porosity:  
656 *Geothermics*, v. 53, p. 255–269, doi:10.1016/j.geothermics.2014.06.003.

657 Evans, T. R., 1977, Thermal Properties of North Sea Rocks.: *Log Analyst*, v. 18, no. 2, p. 3–12.

658 Frost, B. R., and P. N. Shive, 1986, Magnetic mineralogy of the lower continental crust: *Journal*  
659 *of Geophysical Research*, v. 91, no. B6, p. 6513, doi:10.1029/JB091iB06p06513.

660 Fuchs, S., and N. Balling, 2016, Improving the temperature predictions of subsurface thermal  
661 models by using high-quality input data. Part 2: A case study from the Danish-German  
662 border region: *Geothermics*, v. 64, p. 1–14, doi:10.1016/j.geothermics.2016.04.004.

663 Gegenhuber, N., and J. Schoen, 2012, New approaches for the relationship between  
664 compressional wave velocity and thermal conductivity: *Journal of Applied Geophysics*, v.  
665 76, p. 50–55, doi:10.1016/j.jappgeo.2011.10.005.

666 Gladchenko, T. P., J. Skogseid, and O. Eldhom, 1998, Namibia volcanic margin: *Marine*  
667 *Geophysical Researches*, v. 20, no. 4, p. 313–341, doi:10.1023/A:1004746101320.

668 Gosnold, W., and B. Panda, 2002, The Global Heat Flow Database of the International Heat  
669 Flow Commission: doi:http://doi.org/10.17616/R3G305.

670 Goutorbe, B., J. Poort, F. Lucazeau, and S. Raillard, 2011, Global heat flow trends resolved  
671 from multiple geological and geophysical proxies: *Geophysical Journal International*, v.  
672 187, no. 3, p. 1405–1419, doi:10.1111/j.1365-246X.2011.05228.x.

673 Grevemeyer, I., and H. Villinger, 2001, Gas hydrate stability and the assessment of heat flow  
674 through continental margins: *Geophysical Journal International*, v. 145, p. 647–660,  
675 doi:ISI:000169428800007.

676 Griffiths, C. M., N. R. Brereton, R. Beausillon, and D. Castillo, 1992, Thermal conductivity  
677 prediction from petrophysical data: a case study: *Geological Applications of Wireline*  
678 *Logs II*, v. 65, no. 1, p. 299–315, doi:10.1144/GSL.SP.1992.065.01.23.

679 Gu, Y., W. Rühaak, K. Bär, and I. Sass, 2017, Using seismic data to estimate the spatial  
680 distribution of rock thermal conductivity at reservoir scale: *Geothermics*, v. 66, p. 61–72,  
681 doi:10.1016/j.geothermics.2016.11.007.

682 Gunn, D. A., L. D. Jones, M. G. Raines, D. C. Entwisle, and P. R. N. Hobbs, 2005, Laboratory  
683 measurement and correction of thermal properties for application to the rock mass:

684 Geotechnical and Geological Engineering, v. 23, no. 6, p. 773–791, doi:10.1007/s10706-  
685 003-3156-6.

686 Haacke, R. R., G. K. Westbrook, and R. D. Hyndman, 2007, Gas hydrate, fluid flow and free gas:  
687 Formation of the bottom-simulating reflector: Earth and Planetary Science Letters, v.  
688 261, no. 3–4, p. 407–420, doi:10.1016/j.epsl.2007.07.008.

689 Hamza, V. M., and F. P. Vieira, 2012, Global distribution of the lithosphere-asthenosphere  
690 boundary: A new look: Solid Earth, v. 3, no. 2, p. 199–212, doi:10.5194/se-3-199-2012.

691 Harper, M. L., 1971, Approximate geothermal gradients in the North Sea basin: Nature, v. 230,  
692 no. 5291, p. 235–236, doi:10.1038/230235a0.

693 Hartmann, A. A., V. Rath, and C. Clauser, 2005, Thermal conductivity from core and well log  
694 data: International Journal of Rock Mechanics and Mining Sciences, v. 42, no. 7- 8 SPEC.  
695 ISS., p. 1042–1055, doi:10.1016/j.ijrmms.2005.05.015.

696 Hasterok, D., 2010, Thermal State of Continental and Oceanic Lithosphere: The University of  
697 Utah, 168 p.

698 Hasterok, D., D. S. Chapman, and E. E. Davis, 2011, Oceanic heat flow: Implications for global  
699 heat loss: Earth and Planetary Science Letters, v. 311, no. 3–4, p. 386–395,  
700 doi:10.1016/j.epsl.2011.09.044.

701 He, L., J. Wang, X. Xu, J. Liang, H. Wang, and G. Zhang, 2009, Disparity between measured and  
702 BSR heat flow in the Xisha Trough of the South China Sea and its implications for the  
703 methane hydrate: Journal of Asian Earth Sciences, v. 34, no. 6, p. 771–780,  
704 doi:10.1016/j.jseaes.2008.11.004.

705 Hodgson, N., A. Intawong, K. Rodriguez, and M. Huuse, 2014, A seismic tool to reduce source  
706 maturity risk in unexplored basins: First Break, v. 32, no. 3, p. 103–108.

707 Hokstad, K., Z. A. Tašárová, S. A. Clark, R. Kyrkjebø, K. Duffaut, C. Fichler, and T. Wiik, 2017,  
708 Radiogenic heat production in the crust from inversion of gravity and magnetic data:  
709 Norsk Geologisk Tidsskrift, v. 97, no. 3, p. 241–254, doi:10.17850/njg97-3-04.

710 Horai, K., 1982, Thermal Conductivity of Sediments and Igneous Rocks Recovered during Deep  
711 Sea Drilling Project Leg 60, *in* D. M. Hussong, and S. Uyeda, eds., Initial Reports of the  
712 Deep Sea Drilling Project, 60: U.S. Government Printing Office, p. 807–834,  
713 doi:10.2973/dsdp.proc.60.149.1982.

714 Hornbach, M. J., W. S. Holbrook, A. R. Gorman, K. L. Hackwith, D. Lizarralde, and I. Pecher,  
715 2003, Direct seismic detection of methane hydrate on the Blake Ridge: Geophysics, v.  
716 68, no. 1, p. 92–100, doi:10.1190/1.1543196.

717 Horner, D. R., 1951, Pressure build-up in wells, *in* 3rd World Petroleum Congress Proceedings:  
718 p. WPC-4135.

719 Hunt, J. M., 1984, Generation and Migration of Light Hydrocarbons: Science, v. 226, no. 4680,  
720 p. 1265–1270, doi:10.1126/science.226.4680.1265.

721 Hyndman, R. D., and J. Jolivet, 1976, Heat Flow Measurements in Deep Crustal Holes on the  
722 Mid-Atlantic Ridge: v. 81, no. 23, p. 4053–4060.

723 Hyndman, R. D., G. D. Spence, R. Chapman, M. Riedel, and R. N. Edwards, 2001, Geophysical  
724 Studies of Marine Gas Hydrate in Northern Cascadia, *in* C. K. Paull, and W. P. Dillon, eds.,  
725 Natural Gas Hydrates: Occurrence, Distribution, and Detection: Washington, D. C., AGU,  
726 p. 273–295, doi:10.1029/GM124p0273.

727 Intawong, A., M. Huuse, K. Rodriguez, N. Hodgson, and M. Negonga, 2015, Further de-risking  
728 source rock maturity in the Luderitz Basin using basin modelling to support the BSR-

729 derived near-surface geotherm: *First Break*, v. 33, no. October, p. 71–76.

730 Jaupart, C., J. C. Mareschal, and L. Larotsky, 2016, Radiogenic heat production in the  
731 continental crust: *Lithos*, v. 262, p. 398–427, doi:10.1016/j.lithos.2016.07.017.

732 Jorand, R., C. Clauser, G. Marquart, and R. Pechinig, 2015, Statistically reliable petrophysical  
733 properties of potential reservoir rocks for geothermal energy use and their relation to  
734 lithostratigraphy and rock composition: The NE Rhenish Massif and the Lower Rhine  
735 Embayment (Germany): *Geothermics*, v. 53, p. 413–428,  
736 doi:10.1016/j.geothermics.2014.08.008.

737 Karner, G. D., and N. W. Driscoll, 1999, Tectonic and stratigraphic development of the West  
738 African and eastern Brazilian Margins: insights from quantitative basin modelling:  
739 Geological Society, London, Special Publications, v. 153, no. 1, p. 11–40,  
740 doi:10.1144/GSL.SP.1999.153.01.02.

741 Kretschmer, K., A. Biastoch, L. Rüpke, and E. Burwicz, 2015, Modeling the fate of methane  
742 hydrates under global warming: *Global Biogeochemical Cycles*, v. 29, no. 5, p. 610–625,  
743 doi:10.1002/2014GB005011.

744 Kukkonen, I. T., and S. Peltoniemi, 1998, Relationships between thermal and other  
745 petrophysical properties of rocks in Finland: *Physics and Chemistry of the Earth*, v. 23,  
746 no. 3, p. 341–349, doi:10.1016/S0079-1946(98)00035-4.

747 Kvenvolden, K. A., and T. D. Lorenson, 2001, The Global Occurrence of Natural Gas Hydrate,  
748 *in* C. K. Paull, and W. P. Dillon, eds., *Natural Gas Hydrates: Occurrence, Distribution, and*  
749 *Detection*: Washington, D. C., AGU, p. 3–18, doi:10.1029/GM124p0003.

750 Langel, R. A., and W. J. Hinze, 1998, The magnetic field of the Earth's lithosphere: the satellite  
751 perspective: Cambridge University Press, 429 p., doi:10.1029/99eo00111.

752 Le, A. N., M. Huuse, J. Redfern, R. L. Gawthorpe, and D. Irving, 2015, Seismic characterization  
753 of a Bottom Simulating Reflection (BSR) and plumbing system of the Cameroon margin,  
754 offshore West Africa: *Marine and Petroleum Geology*, v. 68, p. 629–647,  
755 doi:10.1016/j.marpetgeo.2014.12.006.

756 Li, A., R. J. Davies, and S. Mathias, 2017, Methane hydrate recycling offshore of Mauritania  
757 probably after the last glacial maximum: *Marine and Petroleum Geology*, v. 84, p. 323–  
758 331, doi:10.1016/j.marpetgeo.2017.04.007.

759 Light, M. P. R., M. P. Maslanyj, R. J. Greenwood, and N. L. Banks, 1993, Seismic sequence  
760 stratigraphy and tectonics offshore Namibia: *Tectonics and seismic sequence*  
761 *stratigraphy*, v. 71, no. 1, p. 163–191, doi:10.1144/GSL.SP.1993.071.01.08.

762 Lister, C. R. B., 1972, On the Thermal Balance of a Mid-Ocean Ridge: *Geophysical Journal*  
763 *International*, v. 26, no. 5, p. 515–535, doi:10.1111/j.1365-246X.1972.tb05766.x.

764 Locarnini, R. A. et al., 2013, *WORLD OCEAN ATLAS 2013: Temperature Volume 1*: 52 p.,  
765 doi:10.7289/V55X26VD.

766 Lu, Z., and N. Sultan, 2008, Empirical expressions for gas hydrate stability law, its volume  
767 fraction and mass-density at temperatures 273.15K to 290.15K: *Geochemical Journal*, v.  
768 42, no. 2, p. 163–175, doi:10.2343/geochemj.42.163.

769 Lucazeau, F., 2019, Analysis and Mapping of an Updated Terrestrial Heat Flow Data Set:  
770 *Geochemistry, Geophysics, Geosystems*, v. 20, no. 8, p. 4001–4024,  
771 doi:10.1029/2019GC008389.

772 Lucazeau, F., F. Brigaud, and J. L. Bouroulllec, 2004, High-resolution heat flow density in the  
773 lower Congo basin: *Geochemistry, Geophysics, Geosystems*, v. 5, no. 3, p. Q03001,

774 doi:10.1029/2003GC000644.

775 Macgregor, D. S., 2020, Regional variations in geothermal gradient and heat flow across the  
776 African plate: *Journal of African Earth Sciences*, v. 171, p. 103950,  
777 doi:10.1016/j.jafrearsci.2020.103950.

778 Magoon, L. B., and W. G. Dow, 1994, The Petroleum System: Chapter 1: Part I. Introduction,  
779 *in The Petroleum System--From Source to Trap: AAPG Memoir*, p. 3–24.

780 McCarthy, K., K. Rojas, M. Niemann, D. Palmowski, K. Peters, and A. Stankiewicz, 2011, Basic  
781 Petroleum Geochemistry for Source Rock Evaluation: *Oilfield Review*, v. 23, no. 2, p. 32–  
782 43.

783 Mello, M. R., A. A. Bender, N. C. A. Filho, S. Barbanti, M. R. Franke, and C. L. C. Jesus, 2011,  
784 Correlation of the Petroleum System from Santos and Namibian Offshore Basins, *in OTC*  
785 *Brasil: Offshore Technology Conference*, p. 1–16, doi:10.4043/22813-MS.

786 Mielke, P., K. Bär, and I. Sass, 2017, Determining the relationship of thermal conductivity and  
787 compressional wave velocity of common rock types as a basis for reservoir  
788 characterization: *Journal of Applied Geophysics*, v. 140, p. 135–144,  
789 doi:10.1016/j.jappgeo.2017.04.002.

790 Minshull, T. A., 2011, Some comments on the estimation of geothermal gradients from the  
791 depths of bottom simulating reflectors, *in Proceedings of the 7th international*  
792 *conference on gas hydrates*: p. 1–8.

793 Nadeau, P. H., 2011, Earth’s energy “Golden Zone”: a synthesis from mineralogical research:  
794 *Clay Minerals*, v. 46, no. 1, p. 1–24, doi:10.1180/claymin.2011.046.1.1.

795 Paganoni, M., J. A. Cartwright, M. Foschi, R. C. Shipp, and P. Van Rensbergen, 2016, Structure  
796 II gas hydrates found below the bottom-simulating reflector: *Geophysical Research*  
797 *Letters*, v. 43, no. 11, p. 5696–5706, doi:10.1002/2016GL069452.

798 Phrampus, B. J., R. N. Harris, and A. M. Tréhu, 2017, Heat flow bounds over the Cascadia  
799 margin derived from bottom simulating reflectors and implications for thermal models  
800 of subduction: *Geochemistry, Geophysics, Geosystems*, v. 18, no. 9, p. 3309–3326,  
801 doi:10.1002/2017GC007077.

802 Popescu, I., M. De Batist, G. Lericolais, H. Nouzé, J. Poort, N. Panin, W. Versteeg, and H. Gillet,  
803 2006, Multiple bottom-simulating reflections in the Black Sea: Potential proxies of past  
804 climate conditions: *Marine Geology*, v. 227, no. 3–4, p. 163–176,  
805 doi:10.1016/j.margeo.2005.12.006.

806 Popov, Y. A., D. F. C. Pribnow, J. H. Sass, C. F. Williams, and H. Burkhardt, 1999,  
807 Characterization of rock thermal conductivity by high-resolution optical scanning:  
808 *Geothermics*, v. 28, no. 2, p. 253–276, doi:10.1016/S0375-6505(99)00007-3.

809 Popov, Y., V. Tertychnyi, R. Romushkevich, D. Korobkov, and J. Pohl, 2003, Interrelations  
810 Between Thermal Conductivity and Other Physical Properties of Rocks: Experimental  
811 Data: *Pure and Applied Geophysics*, v. 160, no. 5, p. 1137–1161,  
812 doi:10.1007/PL00012565.

813 Pribnow, D. F. C., M. Kinoshita, and C. . Stein, 2000, Thermal data collection and heat flow  
814 recalculations for ODP Legs 101-180: 1–25 p.

815 Priyanto, B., 2018, Heat Flow Estimation from BSR: An Example from the Aru Region, Offshore  
816 West Papua, Eastern Indonesia, *in Proc. Indonesian petrol. Assoc., 39th Ann. Conv.:*  
817 *Indonesian Petroleum Association (IPA)*, p. 11, doi:10.29118/IPA.0.15.G.267.

818 Putuhena, H., A. M. W. Newton, J. Cartwright, and M. Huuse, 2021, Middle to late Pleistocene

819 palaeoceanography inferred from ridge-furrow structures on the continental slope  
820 offshore Angola: *Marine Geology*, v. 439, no. July, p. 106562,  
821 doi:10.1016/j.margeo.2021.106562.

822 Rochelle-Bates, N., M. Huuse, S. Schröder, and G. Pritchard, 2017, Seismic Characterisation of  
823 “Prospect B”: A Possible Carbonate Build-Up From the Late Syn-Rift (Barremian) of the  
824 Lüderitz Basin, Namibia, *in* AAPG Annual Convention and Exhibition.

825 Ruppel, C. D., and J. D. Kessler, 2017, The interaction of climate change and methane  
826 hydrates: *Reviews of Geophysics*, v. 55, no. 1, p. 126–168, doi:10.1002/2016RG000534.

827 Samakinde, C. A., J. M. van Bever Donker, R. Durrheim, and M. Manzi, 2021, Hydrocarbon  
828 Generation and Migration From Barremian – Aptian Source Rocks, Northern Orange  
829 Basin, Offshore Western South Africa: a 3D Numerical Modelling Study: *Journal of*  
830 *Petroleum Geology*, v. 44, no. 2, p. 187–208, doi:10.1111/jpg.12785.

831 Sarkar, A. D., 2020, Reflection Seismic Thermometry: University of Manchester, 333 p.,  
832 doi:10.31237/osf.io/fk7pb.

833 Sarkar, A. D., and M. Huuse, 2022, Reflection seismic thermometry: *Basin Research*, v. 34, no.  
834 1, p. 3–24, doi:10.1111/bre.12608.

835 Schicks, J. M., 2018, Gas Hydrates: Formation, Structures, and Properties, *in* H. Wilkes, ed.,  
836 Hydrocarbons, Oils and Lipids: Diversity, Origin, Chemistry and Fate. *Handbook of*  
837 *Hydrocarbon and Lipid Microbiology*: Springer, Cham, p. 81–95,  
838 doi:doi.org/10.1007/978-3-319-54529-5\_2-1.

839 Schmidt, S., 2004, The Petroleum Potential of the Passive Continental Margin of South-  
840 Western Africa – A Basin Modelling Study: Unpublished PhD dissertation, Fakultät für  
841 Georessourcen und Materialtechnik der Rheinisch-Westfälischen Technischen  
842 Hochschule Aachen, Germany., 182 p.

843 Sclater, J. G., C. Jaupart, and D. Galson, 1980, The heat flow through oceanic and continental  
844 crust and the heat loss of the Earth: *Reviews of Geophysics*, v. 18, no. 1, p. 269–311,  
845 doi:10.1029/RG018i001p00269.

846 Serié, C., M. Huuse, N. H. Schødt, J. M. Brooks, and A. Williams, 2017, Subsurface fluid flow in  
847 the deep-water Kwanza Basin, offshore Angola: *Basin Research*, v. 29, no. 2, p. 149–179,  
848 doi:10.1111/bre.12169.

849 Shankar, U., and M. Riedel, 2013, Heat flow and gas hydrate saturation estimates from  
850 Andaman Sea, India: *Marine and Petroleum Geology*, v. 43, p. 434–449,  
851 doi:10.1016/j.marpetgeo.2012.12.004.

852 Shipley, T. H., and M. H. Houston, 1979, Seismic Evidence for Widespread Possible Gas  
853 Hydrate Horizons on Continental Slopes and Rises: *AAPG Bulletin*, v. 63, no. 12, p. 2204–  
854 2213, doi:10.1306/2F91890A-16CE-11D7-8645000102C1865D.

855 Sloan, E. D., S. Subramanian, P. N. Matthews, J. P. Lederhos, and A. A. Khokhar, 1998,  
856 Quantifying Hydrate Formation and Kinetic Inhibition: *Industrial & Engineering*  
857 *Chemistry Research*, v. 37, no. 8, p. 3124–3132, doi:10.1021/ie970902h.

858 Van Der Spuy, D., 2003, Aptian source rocks in some South African Cretaceous basins:  
859 *Geological Society, London, Special Publications*, v. 207, no. 1, p. 185–202,  
860 doi:10.1144/GSL.SP.2003.207.10.

861 Stoll, R. D., and G. M. Bryan, 1979, Physical properties of sediments containing gas hydrates:  
862 *Journal of Geophysical Research*, v. 84, no. B4, p. 1629–1634,  
863 doi:10.1029/JB084iB04p01629.

864 Thompson, K. F. ., 1979, Light hydrocarbons in subsurface sediments: *Geochimica et*  
865 *Cosmochimica Acta*, v. 43, no. 5, p. 657–672, doi:10.1016/0016-7037(79)90251-5.

866 Tissot, B. P., R. Pelet, and P. H. Ungerer, 1987, Thermal History of Sedimentary Basins,  
867 Maturation Indices, and Kinetics of Oil and Gas Generation: *AAPG Bulletin*, v. 71, no. 12,  
868 p. 1445–1466, doi:10.1306/703C80E7-1707-11D7-8645000102C1865D.

869 Torsvik, T. H., S. Rouse, C. Labails, and M. A. Smethurst, 2009, A new scheme for the opening  
870 of the South Atlantic Ocean and the dissection of an Aptian salt basin: *Geophysical*  
871 *Journal International*, v. 177, no. 3, p. 1315–1333, doi:10.1111/j.1365-  
872 246X.2009.04137.x.

873 Waite, W. F. et al., 2009, Physical properties of hydrate-bearing sediments: *Reviews of*  
874 *Geophysics*, v. 47, no. 4, p. RG4003, doi:10.1029/2008RG000279.

875 Wanke, A. W., and R. Toirac-proenza, 2018, Seismic Architecture of Outer Shelf Canyon  
876 Segments in the Lüderitz Basin, Offshore Namibia, *in* 2018 AAPG International  
877 Conference and Exhibition: doi:10.1306/11222Wanke2019.

878 Wefer, G., W. H. Berger, and C. Richter, 1998, Site 1084, *in* G. Wefer, W. H. Berger, and C.  
879 Richter, eds., *Proceedings of the Ocean Drilling Program 175 Initial Reports: Ocean*  
880 *Drilling Program*, p. 339–384, doi:10.2973/odp.proc.ir.175.112.1998.

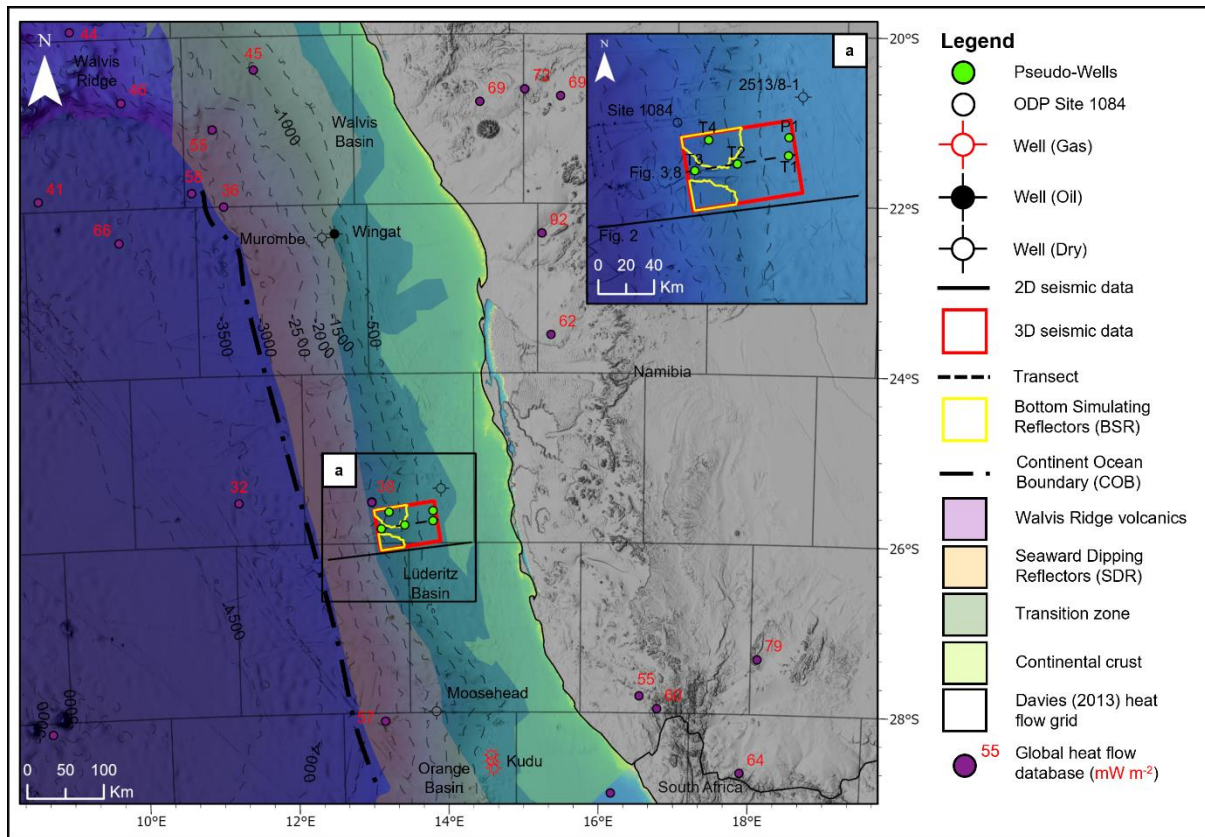
881 Wood, W. T., and C. Ruppel, 2000, Seismic and thermal investigations of the Blake Ridge gas  
882 hydrate area: A synthesis, *in* C. K. Paull, R. Matusmoto, P. J. Wallace, and W. P. Dillon,  
883 eds., *Proceedings of the Ocean Drilling Program: Scientific Results*: p. 253–264,  
884 doi:10.2973/odp.proc.sr.164.203.2000.

885 Yamano, M., S. Uyeda, Y. Aoki, and T. H. Shipley, 1982, Estimates of heat flow derived from  
886 gas hydrates: *Geology*, v. 10, no. 7, p. 339, doi:10.1130/0091-  
887 7613(1982)10<339:EOHFDF>2.0.CO;2.

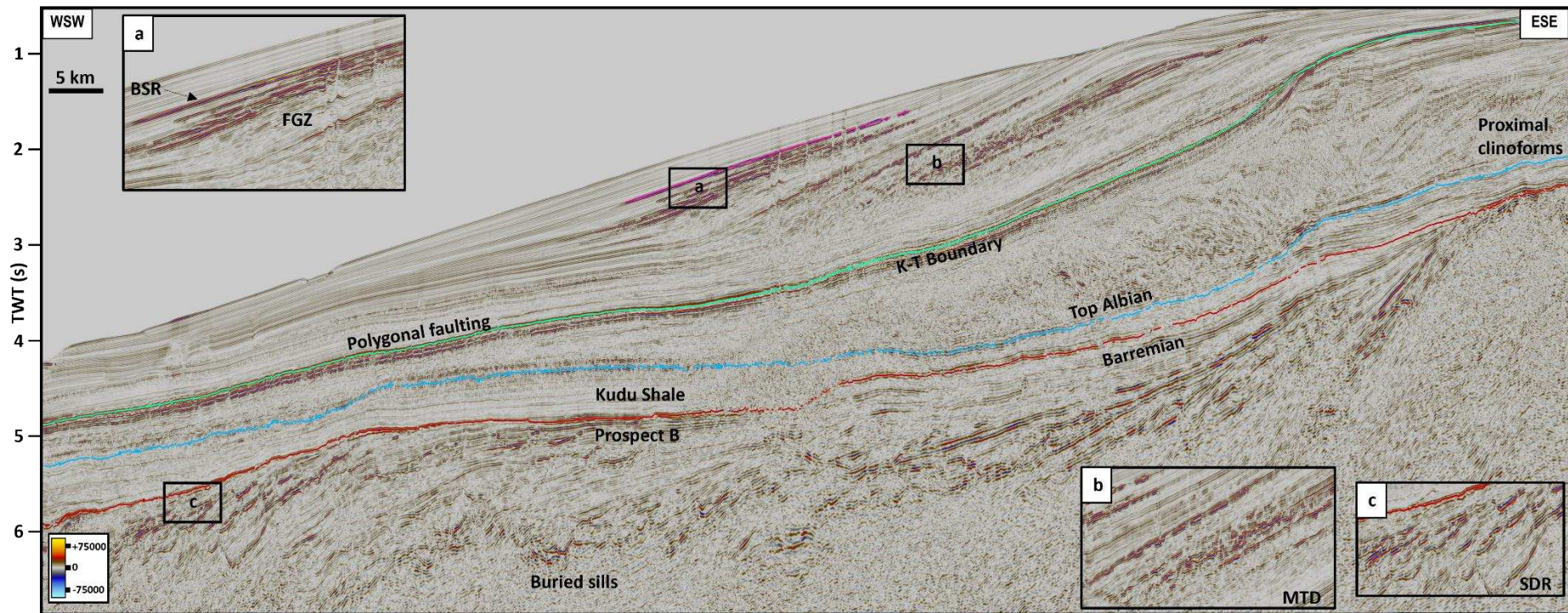
888 Zamora, M., D. Vo-Thanh, G. Bienfait, and J. P. Poirier, 1993, An empirical relationship  
889 between thermal conductivity and elastic wave velocities in sandstone: *Geophysical*  
890 *Research Letters*, v. 20, no. 16, p. 1679–1682, doi:10.1029/92GL02460.

891

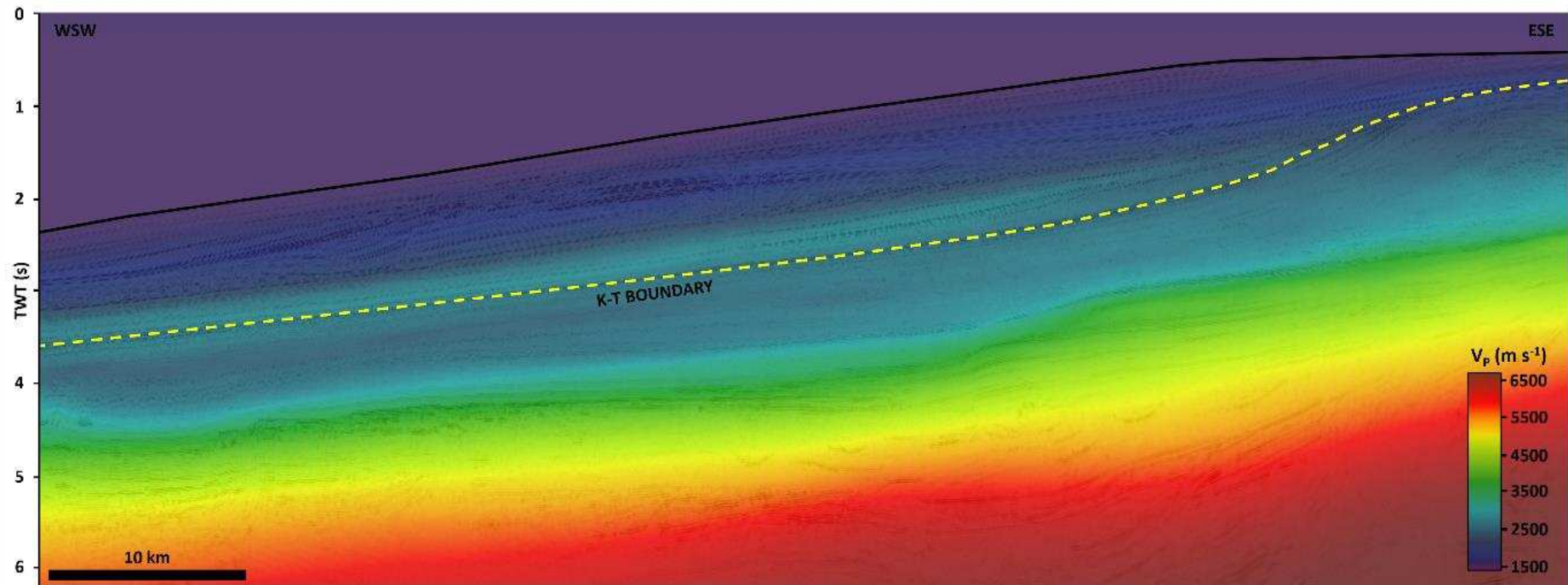
892 Figure captions



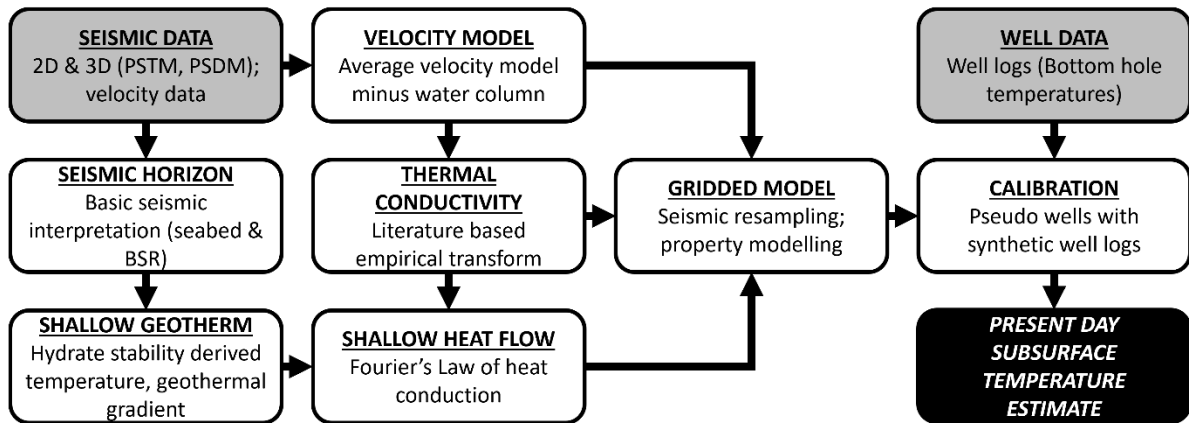
893  
 894 *Figure 1: Location map displaying Lüderitz Basin area of interest with available seismic data,*  
 895 *using UTM Zone 33 S projection. Key geological, structural and bathymetric features offshore*  
 896 *Namibia are highlighted (contour intervals of 500 m [ $\sim$ 1640 ft]), adapted from (Bray et al.,*  
 897 *1998; Gladczenko et al., 1998; Becker et al., 2009). (a) Inset map displaying extent of seismic*  
 898 *data available, mapped BSRs, modelled pseudo-wells and transects along which modelling*  
 899 *has been conducted. Example open source global heat flow databases are shown in the form*  
 900 *of borehole data (Gosnold and Panda, 2002) and Davies (2013) heat flow grid. Regional*  
 901 *exploration wells in neighbouring Walvis & Orange Basins are shown for context.*  
 902



903  
 904 *Figure 2: Stratigraphic dip (WSW-ESE) transect displaying two-way travel time (TWT) seismic reflection structure in the Lüderitz Basin.*  
 905 *Features visible include clinoforms in near shore section, with (a) BSR, free gas zone (FGZ) below it highlighted by bright reflections (associated*  
 906 *with gas) and mass transport features in Tertiary section. (b) Close up of shallow Cenozoic sediments displaying mass transport deposit (MTD)*  
 907 *complexes. Cretaceous – Tertiary (K-T) boundary is marked by intense polygonal faulting. In the deeper Mesozoic section, intrusive sills are*  
 908 *observable beneath a mounded platform like structure (speculated to be a Barremian carbonate reef) (Rochelle-Bates et al., 2017) overlain by*  
 909 *Aptian age “Kudu Shale” source rock interval. (c) Close up of seaward dipping reflectors (SDRs) at depth in the distal section 2D seismic line (Fig.*  
 910 *1a).*



911  
 912 *Figure 3: WSE-ENE transect (Fig. 1a) of seismic reflection volume in time domain overlain with interval velocities and K-T boundary highlighted.*  
 913 *Velocities near seabed (indicated by the black line) are low (close to water, i.e. 1.5 km/s). Overall deepwater Tertiary section is characterised by*  
 914 *low velocities. Velocity inversion seen near K-T boundary (yellow dashed line). K-T = Cretaceous-Tertiary.*

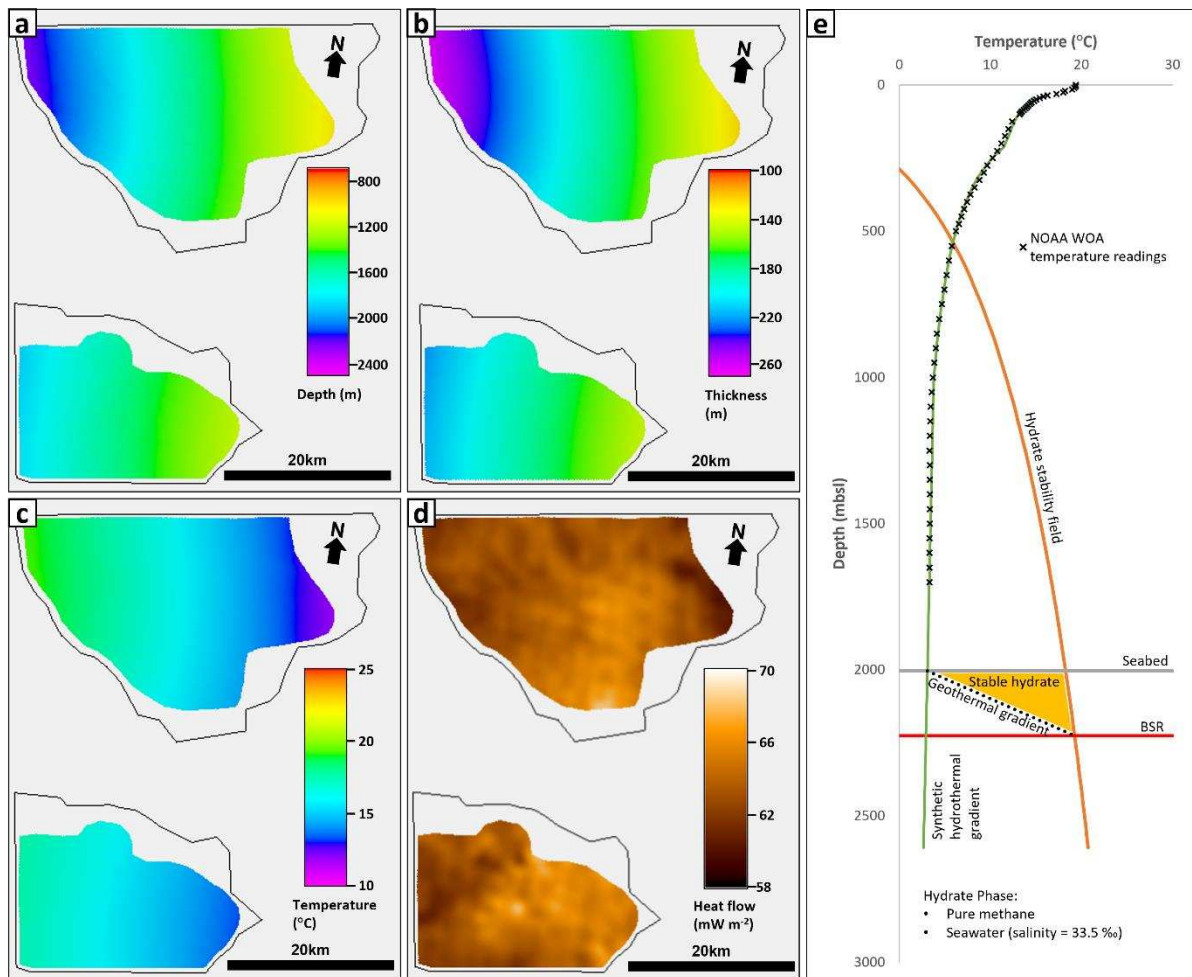


915  
916 *Figure 4: Schematic summary of the steps involved as part of the reflection seismic*  
917 *thermometry methodology used in this study (adapted from (Sarkar, 2020). PSTM = Post*  
918 *Stack Time Migrated; PSDM = Post Stack Depth Migrated; BSR = Bottom Simulating*  
919 *Reflector.*

920



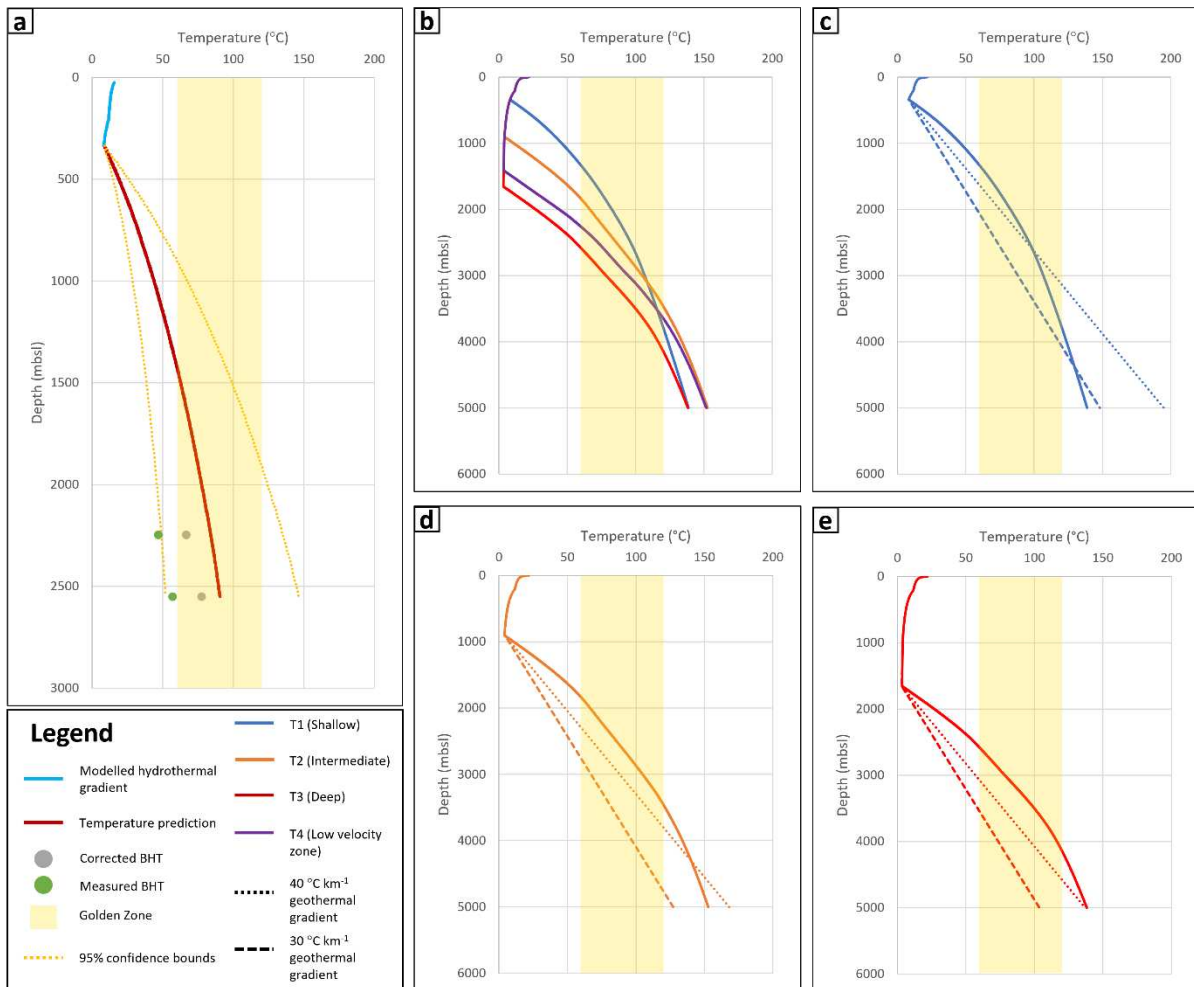
921  
922 *Figure 5: Empirical velocity to thermal conductivity transform utilising experimental datasets*  
923 *from published literature. These measurements are made on samples in laboratory*  
924 *conditions and represent a wide range of lithologies. Furthermore, only results from wet*  
925 *sample measurements are displayed, as the transform will be applied in the shallow*  
926 *subsurface where there is very likely to be fluid fill (for example the GHSZ). Measurements*  
927 *were made using transient method (using optical scanning equipment). GHSZ = Gas hydrate*  
928 *stability zone.*



930

931 *Figure 6: BSR attributes (a – depth; b – GHSZ thickness; c – temperature at base of GHSZ; & e*  
 932 *– heat flow) are displayed for high confidence area only, with black polygon representing*  
 933 *whole BSR interpretation on seismic. (d) Hydrate stability diagram for a pure methane-*  
 934 *seawater system, used to compute temperature at the phase boundary (Fig. 6c). A synthetic*  
 935 *hydrothermal gradient is shown, computed using the annualised mean temperature data*  
 936 *points from the 1 degree resolution dataset of the WOA (Locarnini et al., 2013). The hydrate*  
 937 *stability zone has an average thickness of 184 m (~604 ft) as observed within the study area*  
 938 *(Fig. 6b). The cumulative area of both the mapped BSRs is  $0.941 \cdot 10^9 \text{ m}^2$  ( $\sim 1.01 \cdot 10^{10} \text{ ft}^2$ ).*  
 939 *Assuming all the sediment above the BSRs contain gas hydrate, a typical hydrate saturation*  
 940 *of 10 % (Waite et al., 2009) would yield a potential methane hydrate volume of  $1.73 \cdot 10^{10} \text{ m}^3$*   
 941 *( $\sim 6.11 \cdot 10^{11} \text{ ft}^3$ ). BSR = Bottom Simulating Reflector; GHSZ = Gas Hydrate Stability Zone;*  
 942 *WOA = World Ocean Atlas.*

943



944

945

946

947

948

949

950

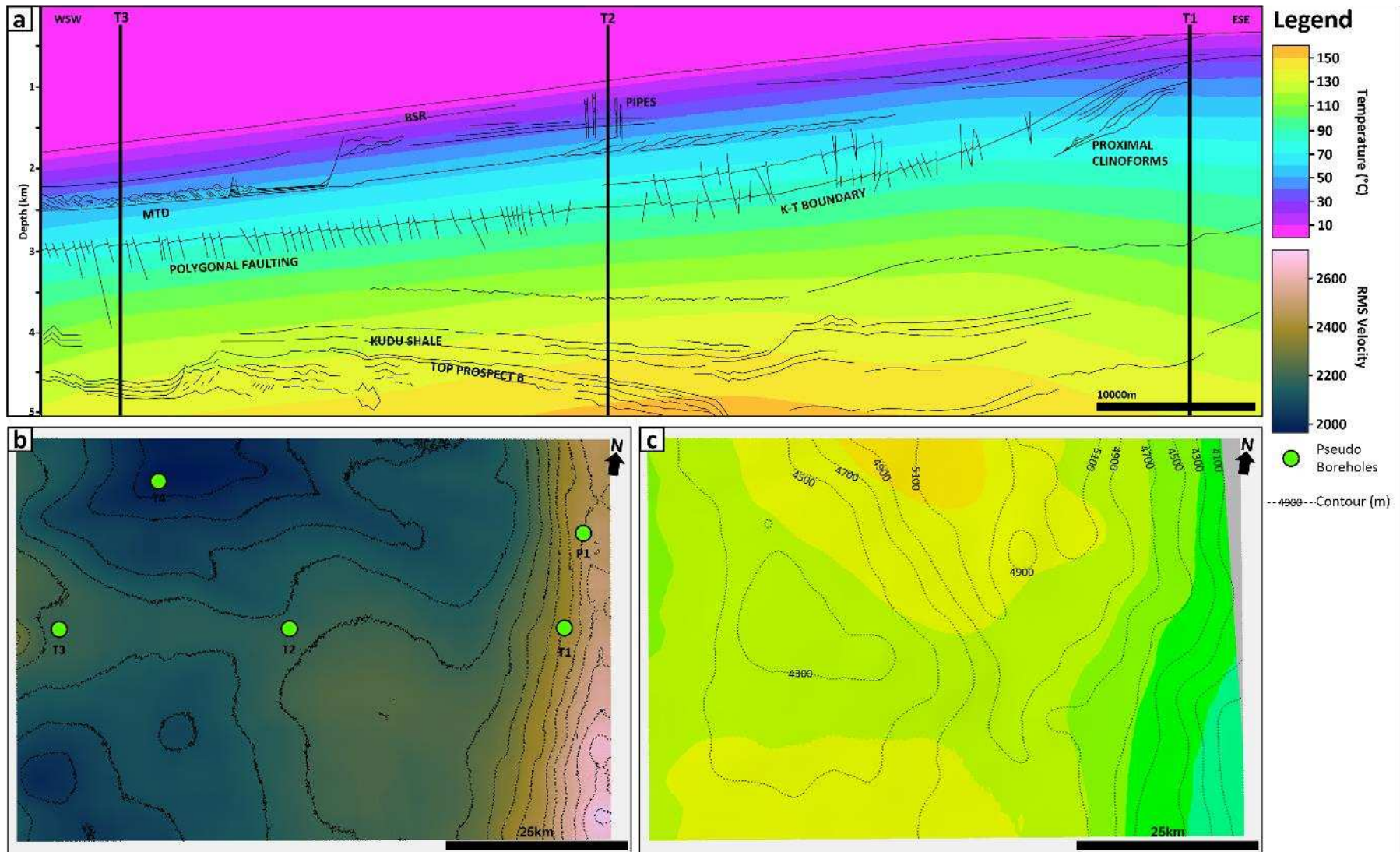
951

952

953

954

Figure 7: Modelled temperature for 2513/8-1 against measured and corrected borehole temperatures, with Golden Zone interval overlain for reference. (a) Thermal profile for pseudo-well P1 simulating 2513/8-1 with corrected and uncorrected BHT readings. 95% confidence upper and lower bounds are also displayed. (b) Thermal profile for pseudo-wells T1-T4. (c) T1 shallow water thermal profile with modelled linear geothermal gradients. (d) T2 intermediate water depth thermal profile with modelled linear geothermal gradients. (e) T3 deep water thermal profile with modelled linear geothermal gradients. (c-e) Modelling subsurface temperature with typical linear geothermal gradients highlights the variability in depth expected for the Golden Zone. BHT = Bottom hole temperature.



955

956

957 *Figure 8: (a) Depth profile of temperature predicted from reflection seismic thermometry.*  
958 *Pseudo-wells corresponding to shallow, intermediate, and deep water are marked. (b) RMS*  
959 *velocity extraction of interval velocities (for interval up to 2 s below seabed) highlighting the*  
960 *zone of low velocities encountered below, in particular, the Northern BSR. Pseudo-well T4 is*  
961 *placed to illustrate this. (c) Temperature prediction from the model mapped across the base*  
962 *of the Aptian source rock above the mounded structure referred to as Prospect B (Fig. 2c).*  
963 *The thermal model produced was used to interrogate the predicted present-day temperature*  
964 *for the base of the source rock interval as shown in Fig. 2c. The temperature ranged between*  
965 *93.2 – 157.2 °C [200 – 315 °F] for a depth range of 3400 – 5400 mbsl [~11155 – 17717 ftbsl].*  
966 *Scientific colour bar templates based on (Cramer et al., 2020). RMS = Root Mean Squared;*  
967 *BSR = Bottom Simulating Reflector; mbsl = metres below sea level; ftbsl = feet below sea*  
968 *level.*

969 **Tables**

970 *Table 1: Parameters for BSR derived heat flow bounds, with the hydrate phase, pressure*  
 971 *gradient and seabed temperature kept unchanged. BSR = Bottom Simulating Reflector.*

<b>Sediment velocity (m s<sup>-1</sup>)</b>	<b>Hydrate phase</b>	<b>Thermal conductivity (W m<sup>-1</sup> K<sup>-1</sup>)</b>	<b>Pressure conditions</b>	<b>Seabed temperature</b>	<b>Heat flow bound</b>
<b>Minimum</b>	Pure methane & seawater	Minimum	Hydrostatic	Modelled hydrothermal gradient	Minimum
<b>Maximum</b>	Pure methane & seawater	Maximum	Hydrostatic	Modelled hydrothermal gradient	Maximum

972

973